

Supporting Information

Thermal Defect Engineering of Precious Group Metal-Organic Frameworks: Impact on the Catalytic Cyclopropanation Reaction

Werner R. Heinz,^a Raphael Junk,^a Iker Agirrezabal-Telleria,^b Bart Bueken,^c Hana Bunzen,^d Thorsten Gölz,^a Mirza Cokoja,^a Dirk De Vos,^c and Roland A. Fischer^a

^a Chair of Inorganic and Metal-Organic Chemistry, Department of Chemistry, Technical University of Munich, Lichtenbergstraße 4, 85748 Garching, Germany. E-mail: roland.fischer@tum.de

^b Department of Chemical and Environmental Engineering, Engineering School of the University of the Basque Country (UPV/EHU), Plaza Torres Quevedo 1, 48013 Bilbao, Spain. E-mail: iker.aguirrezabal@ehu.eus

^c Centre for Membrane Separations, Adsorption, Catalysis and Spectroscopy for Sustainable Solutions (CMACs), Department of Microbial and Molecular Systems (M2S), KU Leuven, Celestijnenlaan 200F p.o. box 2461, 3001 Leuven, Belgium. E-mail: dirk.devos@kuleuven.be

^d Chair of Solid State Materials Chemistry, University of Augsburg, Universitätsstraße 1, 86159 Augsburg, Germany. E-mail: hana.bunzen@physik.uni-augsburg.de

Table of Contents

Experimental Details	3
General considerations.....	3
Instrumentation	3
Thermal syntheses.....	3
Powder X-Ray diffraction.....	3
Elemental Analysis.....	4
Gas sorption measurements	4
Fourier-transform infrared spectroscopy.....	4
Raman spectroscopy	4
DFT calculations of Ru- and Rh-paddle-wheel complexes.....	4
Thermogravimetric analysis	5
High-resolution transmission electron microscopy.....	5
Catalytic Experiments.....	6
Additional Information – Material Descriptions.....	7
Definitions for “defect amount or “defectiveness” used in the manuscript.....	7
Structural Complexity in Pristine PGM-MOFs	8
Assumed Reactions during TDE.....	9
Additional Information – Material Characterization	10
Thermal Defect-Engineering – Temperature Program.....	10
Powder X-Ray Diffraction	10
Elemental Analysis & Surface Areas	11
N ₂ Sorption Isotherms & Pore Size Distributions.....	12
Thermogravimetric Analysis.....	13
FT-IR spectroscopy	15
Raman Spectroscopy	17
TGA-Based Titration of OMS using CO	19
Transmission Electron Microscopy.....	22
Additional Information – Cyclopropanation Catalysis.....	26
Mechanistic Aspects relevant for this Study	26
Additional Catalysis Data.....	27

Experimental Details

General considerations

Trimesic acid (Sigma-Aldrich), $\text{RuCl}_3 \cdot x \text{H}_2\text{O}$ (Precious Metals Online), $\text{Rh}_2(\text{OAc})_4$ (Sigma-Aldrich, Carbolution) and HPLC-grade acetone and ethanol (VWR Chemicals) were purchased commercially and used without further purification. Ultra-pure water was obtained using a Milli-Q purification system ($18.2 \text{ M}\Omega \text{ cm}^{-1}$). Dichloromethane was purified and dried using a MBraun SPS-800. $\text{Ru}_2(\text{OAc})_4\text{Cl}$ was synthesized following literature procedures.¹ Desolvated MOFs were handled in a glovebox using argon (>99.996%; Westfalen).

Instrumentation

Thermal syntheses

Post-synthetic treatments of the pristine MOF samples to yield the TDE-MOFs were conducted with a Netzsch TG209 F1 Libra in an argon-filled glovebox. Decomposition gases were analyzed *in-situ* using a Netzsch QMS 403C Aëolos mass spectrometer. The acceleration voltage of the mass spectrometer was set to 2300 V for the most abundant ions ($m/z = 18, 28$ and 44) and to 2800 V for the less abundant ions ($m/z = 2, 14, 16, 25, 30, 31, 35, 37, 46, 56, 58, 60$ and 70). The transfer line, the inlet system and the adapter head were heated to $250 \text{ }^\circ\text{C}$, $200 \text{ }^\circ\text{C}$ and $160 \text{ }^\circ\text{C}$, respectively. Argon served both as the purge gas and the protective gas of the measurement set-up. Flow rates were set to 20 mL min^{-1} . The following heating protocols were used:

Targeted weight loss of 5.5 wt-% (denoted as 10% defects): Ramp from $15 \text{ }^\circ\text{C}$ to $150 \text{ }^\circ\text{C}$, subsequent isothermal equilibration (30 min), ramp to $200 \text{ }^\circ\text{C}$, subsequent isothermal equilibration (30 min), ramp to $220 \text{ }^\circ\text{C}$, subsequent isothermal equilibration (30 min), ramp to $240 \text{ }^\circ\text{C}$, subsequent isothermal equilibration (20 min), ramp to $260 \text{ }^\circ\text{C}$, subsequent isothermal equilibration (20 min).

Targeted weight loss of 10 wt-% and 15 wt-% (denoted as 20% and 30% defects): Ramp from $15 \text{ }^\circ\text{C}$ to $150 \text{ }^\circ\text{C}$, subsequent isothermal equilibration (30 min), ramp to $200 \text{ }^\circ\text{C}$, subsequent isothermal equilibration (20 min), ramp to $250 \text{ }^\circ\text{C}$, subsequent isothermal equilibration (60 min), ramp to $270 \text{ }^\circ\text{C}$, subsequent isothermal equilibration (20 min), ramp to $290 \text{ }^\circ\text{C}$, subsequent isothermal equilibration (60 min).

All ramps were programmed with a heating rate of 10 K min^{-1} . The thermal treatment was terminated as soon as the targeted mass loss had been reached and the material was cooled to room temperature.

Powder X-Ray diffraction

All diffraction patterns were collected on a PANalytical Empyrean equipped with a Cu X-ray tube ($\lambda = 0.154 \text{ nm}$) operated at 45 kV and 40 mA in a 2θ range of $5\text{-}50^\circ$ in steps of 0.0065651° (2θ) with 0.175 s/step . The incident beam was focussed on the sample through a focusing beam mirror with a $1/8^\circ$ divergence slit and a nickel beta filter (0.2 mm). A PIXcel1D detector was used in receiving mode with a $1/8^\circ$ anti-scatter slit and 0.04 rad soller slits. The activated samples were filled in borosilicate capillaries of 0.5 mm inner diameter and mounted onto a capillary spinner.

Elemental Analysis

Determination of the elemental composition was performed together with the microanalytical laboratories of the chemistry department at the Technical University of Munich. Determination of C, H, N and S was carried out with a Hekatech EuroEA elemental analyser. Metal contents were derived from TGA-based metal oxide residues as reported earlier.² Chlorine contents were determined by potentiometric titration of HCl after thermal decomposition.

Calculation of the sum formula

Based on determined elemental contents and assuming exclusively the oxygen mass fraction missing to complete the 100 wt-%, sum formulas were calculated and normalized to three metal atoms per repeating unit. The GRG nonlinear solver function implemented in *Microsoft Excel*[®] was used for compositional fittings assuming acetate and BTC as the only organic framework components of the pristine MOF samples. To account for BTC decarboxylation in TDE-MOFs, isophthalate (IPA) was added to this protocol optimizing the fitting results. For TDE-MOFs, the ceiling amounts of IPA + BTC and OAc⁻ was restricted to the respective parental BTC and OAc⁻ amounts. It should be mentioned, that other efforts to determine organic ligand ratios (BTC to acetate) have not been successful as typical sample digestions in diluted acids do not proceed quantitatively and paramagnetic ruthenium obstruct qNMR. MAS-NMR of (100/0) sample was used to confirm the general viability of the fitting approach.

Gas sorption measurements

Sorption experiments were conducted using a Micromeritics 3Flex with each 20 to 80 mg of desolvated sample. Prior to the measurement each sample was additionally degassed at 150°C for >10h. Nitrogen isotherms were recorded at 77 K. The BET surface area was calculated using data points in the relative pressure range of 0.01 to 0.1 in the adsorption branch with the *Rouquerol* consistency criteria considered.

Fourier-transform infrared spectroscopy

FT-IR spectra were recorded from finely ground activated powder samples under argon atmosphere in a glovebox using a Bruker ALPHA FTIR spectrometer equipped with a Pt attenuated total reflectance (ATR) unit at room temperature in the range of 400 to 4000 cm⁻¹ with a resolution of 2 cm⁻¹ and 24 scans per measurement. A pyroelectric deuterated L-alanine doped triglycine sulfate (RT-DLaTGS) detector was used.

Raman spectroscopy

Raman spectroscopy was measured with an inVia Reflex Raman System with an optical microscope (Leica DM2700M, 50x magnification) coupled to a Renishaw R04 Raman spectrometer with 532 nm laser wavelength (Laser: RL532C, Class 3B) with activated samples filled into Borosilicate glass capillaries (0.5 mm inner diameter) under argon atmosphere. A Renishaw 266n10 detector was used. All samples were measured with 10 s exposure time, 1 % laser power and 10 accumulations.

DFT calculations of Ru- and Rh-paddle-wheel complexes

All calculations have been performed with the Gaussian 16 suite of software⁴. The level of theory included the use of the hybrid DFT functional B3LYP together with the basis set 6-31+G** for C,H,O, Cl.^{5,6} Ru and Rh have been described by the Stuttgart-Dresden97-ECP⁷.

All structures have been optimized until no negative frequencies have been calculated by frequency analysis. Frequencies calculation have been also used to determine unscaled frequencies and IR and Raman intensities. UV-VIS spectra of selected singlet state compounds have been calculated by time-dependent DFT⁸ taking into account the three most probable electron transitions to singlet and triplet excited states.

4. Gaussian 16, Revision B.01, M. J. Frisch, G. W. Trucks, H. B. Schlegel, G. E. Scuseria, M. A. Robb, J. R. Cheeseman, G. Scalmani, V. Barone, G. A. Petersson, H. Nakatsuji, X. Li, M. Caricato, A. V. Marenich, J. Bloino, B. G. Janesko, R. Gomperts, B. Mennucci, H. P. Hratchian, J. V. Ortiz, A. F. Izmaylov, J. L. Sonnenberg, D. Williams-Young, F. Ding, F. Lipparini, F. Egidi, J. Goings, B. Peng, A. Petrone, T. Henderson, D. Ranasinghe, V. G. Zakrzewski, J. Gao, N. Rega, G. Zheng, W. Liang, M. Hada, M. Ehara, K. Toyota, R. Fukuda, J. Hasegawa, M. Ishida, T. Nakajima, Y. Honda, O. Kitao, H. Nakai, T. Vreven, K. Throssell, J. A. Montgomery, Jr., J. E. Peralta, F. Ogliaro, M. J. Bearpark, J. J. Heyd, E. N. Brothers, K. N. Kudin, V. N. Staroverov, T. A. Keith, R. Kobayashi, J. Normand, K. Raghavachari, A. P. Rendell, J. C. Burant, S. S. Iyengar, J. Tomasi, M. Cossi, J. M. Millam, M. Klene, C. Adamo, R. Cammi, J. W. Ochterski, R. L. Martin, K. Morokuma, O. Farkas, J. B. Foresman, and D. J. Fox, Gaussian, Inc., Wallingford CT, **2016**.
5. a) A.D. Becke, *J. Chem. Phys.* **1993**, *98*, 5648-5652; b) C. Lee, W. Yang, R.G. Parr, *Phys. Rev. B* **1988**, *37*, 785-789; c) S.H. Vosko, L. Wilk, M. Nusair, *Can. J. Phys.* **1980**, *58*, 1200-1211; d) P.J. Stephens, F.J. Devlin, C.F. Chabalowski, M.J. Frisch, *J.Phys.Chem.* **1994**, *98*, 11623-11627.
6. a) W.J. Hehre, R. Ditchfield and J.A. Pople, *J. Chem. Phys.* **1972**, *56*, 2257-2261 (1972); b) T. Clark, J. Chandrasekhar, G. W. Spitznagel, and P. v. R. Schleyer, *J. Comp. Chem.*, **1983**, *4*, 294-301; c) M.M. Francl, W.J. Pietro, W.J. Hehre, J.S. Binkley, M.S. Gordon, D.J. DeFrees and J.A. Pople, *J. Chem. Phys.* **1982**, *77*, 3654-3665.
7. a) A. Bergner, M. Dolg, W. Kuechle, H. Stoll, H. Preuss, *Mol. Phys.* **1993**, *80*,1431-1441 ; b) M. Kaupp, P. v. R. Schleyer, H. Stoll, H. Preuss, *J. Chem. Phys.* **1991**, *94*, 1360-1366; c) M. Dolg, H. Stoll, H. Preuss, R.M. Pitzer, *J. Phys. Chem.* **1993**, *97*, 5852-5859.
8. a) R. E. Stratmann, G. E. Scuseria, M. J. Frisch, *J. Chem. Phys.*, **1998**, *109*, 8218-24. b) F. Furche and R. Ahlrichs, *J. Chem. Phys.*, **2002**, *117*, 7433-7447.

Thermogravimetric analysis

Thermal analysis of the materials was determined with a Mettler Toledo TGA/DSC 1 in aluminium oxide crucibles (70 μ L with lid) with sample amounts of 1 to 5 mg. Samples of activated materials were taken under inert conditions in a glovebox and transferred to the measurement chamber in screw capped vials immediately prior to the measurement. The following thermal program was applied using synthetic air (20 mL min⁻¹, Westfalen, 80% N₂; 20% O₂): At 30 °C isothermal equilibration (15 min), ramp from 30 °C to 700 °C with 10 K min⁻¹, at 700 °C isothermal equilibration (15 min).

High-resolution transmission electron microscopy

TEM and STEM micrographs and EDS elemental mappings were recorded with a JEM NEOARM microscope (JEOL) with a cold FEG electron source operated at 200 kV. Samples were prepared by depositing a drop of the crystalline products dispersed in ethanol onto carbon-coated copper grids (200 mesh) and dried in air.

Catalytic Experiments

4.0 to 5.0 mg MOF material (referring to ≈ 1.3 mol-% catalyst loading) was weighed directly into a 20 mL glass vial in an argon-filled glovebox with a *Sartorius Entris* laboratory balance. The vial was then equipped with a cross-shaped stir bar and sealed using a polypropylene screw cap with a PTFE/silicone septum. A second empty vial was equipped with a stir bar and sealed accordingly. Outside the glovebox, 2.4 mL styrene, 2.4 mL dichloromethane, 0.2 mL toluene and 0.2 mL EDA solution (containing ≥ 13 wt-% CH_2Cl_2) were introduced into this empty vial. Dichloromethane and toluene had been degassed by argon purging prior to their use and were stored over activated 3 Å molecular sieves under inert conditions. 0.5 mL styrene and 0.5 mL dichloromethane, both dry and degassed, were introduced into the vial containing the MOF sample. The contents of both vials were stirred for approximately 20 min at 150 min^{-1} before the entire EDA solution was drawn up into a 5 mL syringe. Using a New Era Pump Systems NE-1010 syringe pump, which was set to a syringe diameter of 12.52 mm and an addition rate of $0.087 \text{ mL min}^{-1}$, the EDA solution was drop-wise introduced into the vial containing the MOF sample over 60 min. A long syringe needle was used to release the pressure that would otherwise build up by the formation of dinitrogen. The first sample was taken when the addition process had been completed, 60 min after starting the syringe pump. This moment was defined as the starting point of the time scale (0 h). Subsequent samples were taken at 20 min, 40 min, 60 min, 2 h, 3 h, 4 h and 24 h. The sampling process was performed by drawing 0.7 mL HPLC grade dichloromethane up into a 1 mL syringe and then taking a 0.1 mL aliquot of the reaction mixture by pulling the plunger to the 0.8 mL mark. The resulting suspension was filtered into a GC vial using a 13 mm PTFE membrane syringe filter with a pore size of $0.2 \mu\text{m}$. Reusability experiments were conducted in a similar way using the same MOF catalyst for five cycles. Every sampling was conducted after 4 h of reaction time. Catalytic parameters were calculated using the following formulae: The conversion X was calculated

using
$$X = \frac{\Sigma n_{\text{products, normalized}}}{\Sigma n_{\text{products, normalized}} + n_{\text{EDA, normalized}}}$$
 with the sum (Σ) of product moles being $n = \frac{I_{\text{GC}}}{\#_{\text{carbon}}}$ comprising the GC-based intensity (I) of each product divided by its carbon number ($\#_{\text{carbon}}$).

Chemoselectivities S were calculated using
$$S = \frac{n_{\text{product}}}{\Sigma n_{\text{products}}}$$
 with the amount n of the particular product divided by the sum of all product amounts. Similarly, diastereoselectivities (DS) are calculated relating

to the trans product as follows:
$$DS_{\text{trans}} = \frac{I_{\text{trans}}}{I_{\text{trans}} + I_{\text{cis}}}$$
 being irrespective of any normalization as both diastereoisomers contain identical carbon contents. Initial TOFs are calculated according to

$$TOF [h^{-1}] = \frac{X_{t=0\text{min}} \cdot n_{\text{EDA}}}{n_{\text{metal}} \cdot 0.5 h}$$
 using the initial conversion $X_{t=0\text{min}}$, the mean reaction time (0.5 h) of EDA molecules during the EDA addition and the molar ratio of EDA and the total metal content used for the reaction. The internal standard toluene was used to derive a continuity factor f assuring constant molarity of EDA and EDA-derived products during each catalytic run. The continuity factor was

calculated according to
$$f = \frac{n_{\text{toluene, normalized}}}{\Sigma n_{\text{products}} + n_{\text{EDA}}}$$
 and remained constant during each run. This validates the chosen data evaluation as no undetected EDA-derived species emerge.

Additional Information – Material Descriptions

Definitions for “defect amount or “defectiveness” used in the manuscript

In this manuscript, the terms “defectiveness” and “defect amount” are used. Although, Dissegna *et al.* have provided a generally accepted definition of “defect” in a recent review on Defective MOFs, that definition is very general and not sufficiently precise for the work presented herein. For this reason and to prevent the readers from confusion, further explanations shall be provided in the following. A tripartite definition appears most suitable for the point defects discussed herein depending on a.) the sample preparation, b.) the network connectivity and c.) the organometallic perspective.

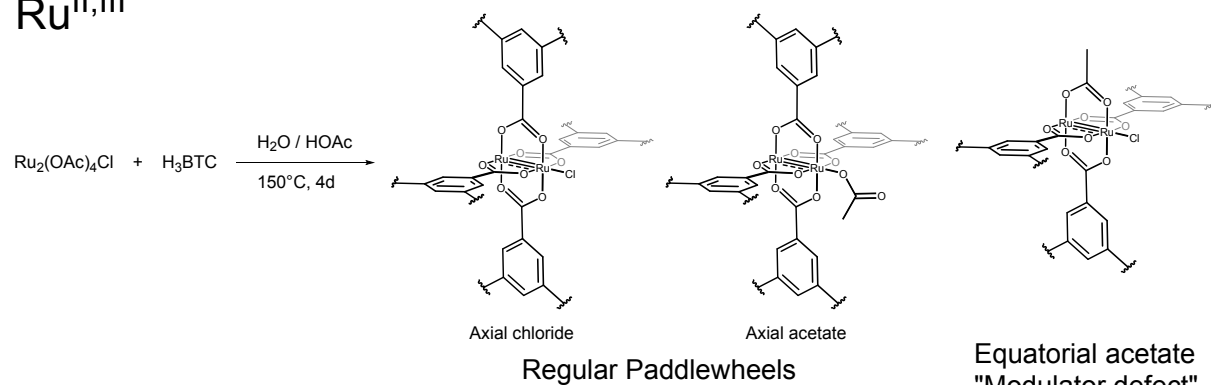
The first definition is related to the experimental procedure and the chosen sample denotation using an (XX/YY) nomenclature. XX refers to the fraction of rhodium PWs as part of the total metal content comprising ruthenium and rhodium (0%, 50% or 100%). YY refers to the **thermally introduced number of defects** (0%, 10%, 20% or 30%). The mentioned values best reflect the defectiveness throughout the three series of TDE materials and results from different calculative approaches (whether a.) the total amount of organics, b.) the ligands or c.) specifically carboxylates are considered). All different values are depicted in Table S3 (see page 11), respectively. In general, thermal treatments result in the removal of exclusively organic constituents (representing ≈50% of the whole framework). Concluded from mass spectrometry, acetate and carbon dioxide are the major components being removed during TDE. There are no indications for the removal of any aromatic fragments. To reach the arbitrarily chosen defectiveness (YY%), weight losses of 5.5, 10 and 15 wt-% were targeted respectively. At this point, it should be mentioned that “defectiveness” in this context quantifies only defects which were introduced to the framework postsynthetically. Defects originating from modulated synthesis and already being present in the pristine samples are not covered in this first definition.

Secondly, the defectiveness of a MOF sample could be qualitatively defined according to the **network connectivity**. In the ideal HKUST-1 structure, each PW is coordinated by four BTC linkers while each of them interconnects three PWs. Modulated synthesis of PGM-MOFs results in relatively large acetate amounts incorporated to the structure. Even if all equatorial coordination sites are occupied, three acetate ligands can replace one BTC linker resulting in a “**connectivity defect**”. Its occurrence has several effects: The lower connectivity hampers the mechanical stability of the framework and its crystallinity. Further the clearly defined size of the micropores is dispersed and mesopore formation (due to missing node defects) occurs. In contrast to decarboxylation of BTC, any removal of monotopic acetates during TDE does not increase the number of these connectivity defects. Since both acetate and aromatic carboxylate ligands have rather similar electronic and steric effects to the metal nodes, strong impacts on the reactivity of PWs is not to be expected for connectivity defects. This situation changes for the **third definition**:

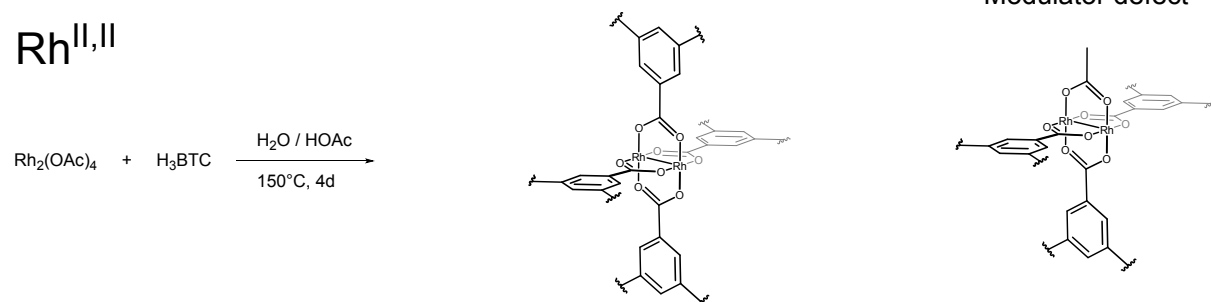
Defects from an organometallic point of view (“**coordination defect**”) are often called ligand vacancies, **open metal sites** (OMS) or coordinatively unsaturated sites (CUS). As usual MOF activation facilitates removal of neutral solvent molecules coordinated to the axial positions of a PW, anionic ligands remain strongly bound. This holds true for axial anions accounting for additional charge compensation in the mixed-valent Ru^{II/III}-BTC but also for equatorial bridging carboxylates. For instance, a connectivity defect according to our second definition is not necessarily considered defective in this third definition as all equatorial metal sites are coordinated with bridging carboxylates. In this work, TDE-induced decarboxylation results in a strong increase in coordination defects. This is accompanied by altered electronic and steric properties such as (partial) metal reduction or increased accessibility of the metal nodes and potential mesopore formation (removal of “pore walls”). Changes in reactivity of these “coordination defects” are observed for instance in ethylene sorption and dimerization.

Structural Complexity in Pristine PGM-MOFs

Ru^{II,III}



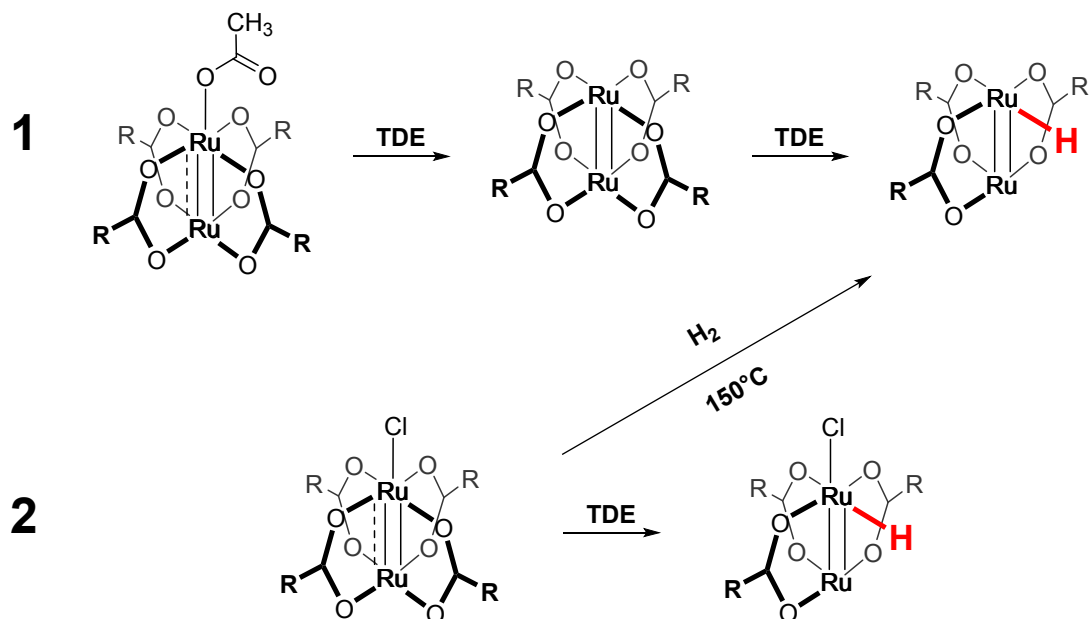
Rh^{II,II}



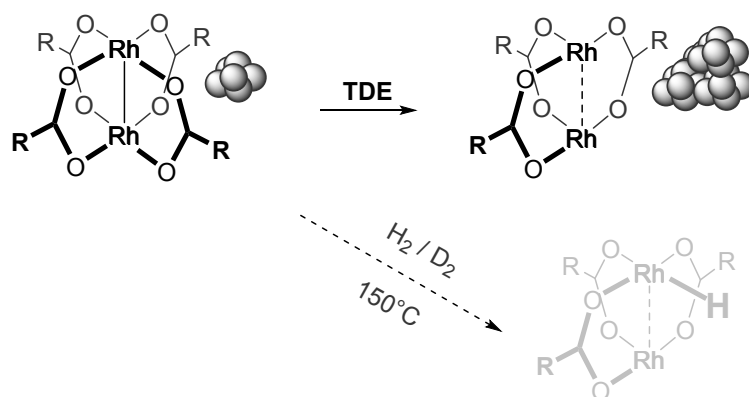
Scheme S 1: Structural complexity in pristine PGM-HKUST-1 derivatives. The mixed-valent Ru-HKUST-1 comprises one axial ligand per PW which is either chloride or acetate for compensation of the additional charge. Modulator-based acetate incorporation on equatorial positions (up to three equatorial acetates per PW) occurs in both metal derivatives.

Assumed Reactions during TDE

a.) Mixed valent Ru-MOF:



b.) Univalent Rh-MOF:



*Scheme S 2: Assumed molecular reactions during TDE of the highly complex PGM-MOFs. Organic residues R represent either CH_3 (acetate) or $\text{C}_6\text{H}_3\text{O}_4$ (BTC). Each univalent PW could carry $x=1-4$ BTC ligands and $4-x$ acetate ligands according to Scheme S1. **a.)** Mixed-valent Ru-MOF. Either acetate (**1**) or chloride (**2**) can coordinate one axial position for charge compensation. **1** displays the case when acetate is the additional axial ligand: Temperature-induced removal first generates a univalent Ru-PW which further undergoes ligand removal/fragmentation under subsequent Ru-H formation. **2** displays the case of an axially bound chloride ligand: TDE under inert atmosphere retains the chloride while hydrogen treatment facilitates its removal. **b.)** The assumed TDE of the univalent Rh-MOF features much less flexibility. While few Rh NPs are already present in the pristine MOF, their agglomeration leads to larger NPs during TDE. No Rh-H formation is observed in inert atmosphere TDE, while low Rh-H formation is visible under harsher H_2 / D_2 treatment. Overall Ru-MOF seems more tolerant towards TDE-induced ligand removal / fragmentation. Hypothetically the higher bond order in Ru dimers allows more progressive ligand removal since M-M bonds could potentially prevent NP formation.*

Additional Information – Material Characterization

Thermal Defect-Engineering – Temperature Program

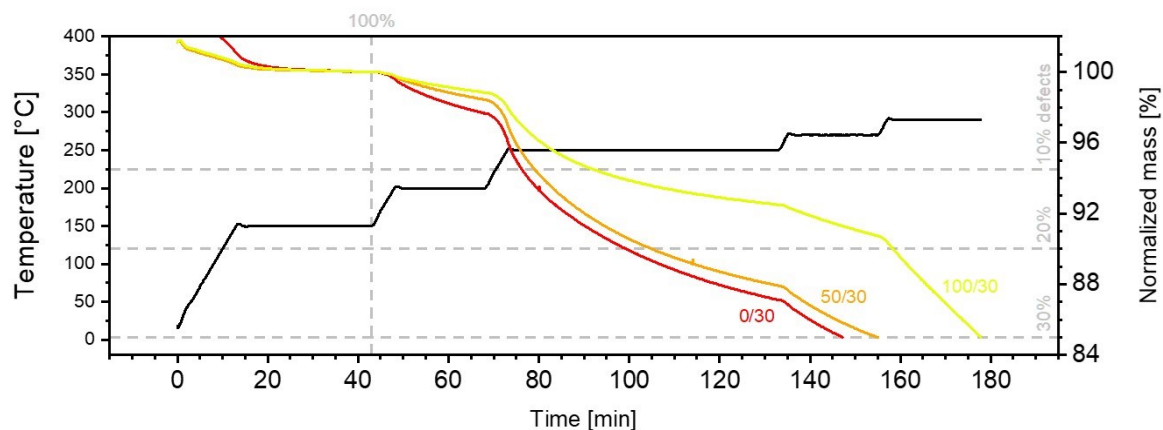


Figure S 1: Weight profiles and the underlying temperature program for TDE-MOF syntheses in 20 mL min^{-1} argon stream. Thermal syntheses were performed in an Ar-filled glovebox to prevent deactivation of generated open metal sites by oxygen or moisture after the treatment. The dashed vertical line indicates the point of weight-referencing. The dashed horizontal lines indicate the targeted weight-loss for 10%, 20% and 30% defect amounts.

Powder X-Ray Diffraction

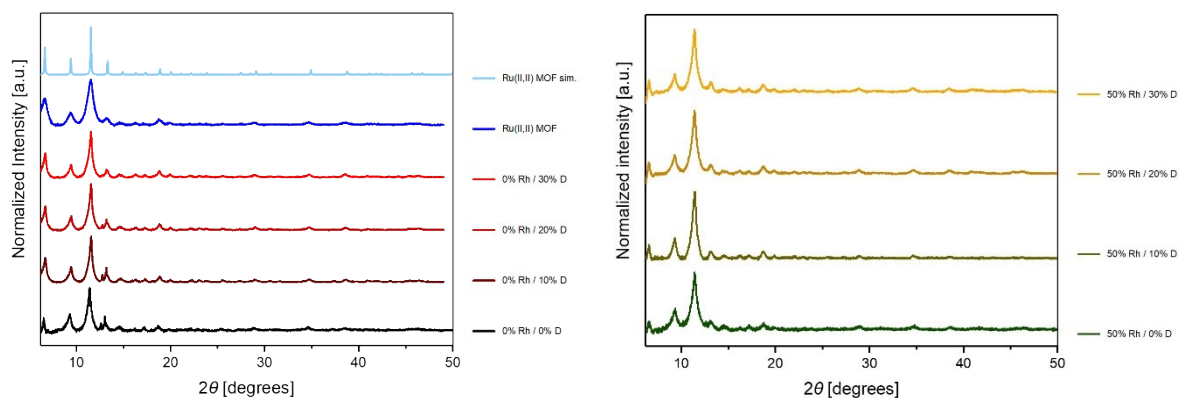


Figure S 2: PXRD patterns of 0%Rh and 50%Rh pristine and TDE-materials indicate preserved crystallinity.

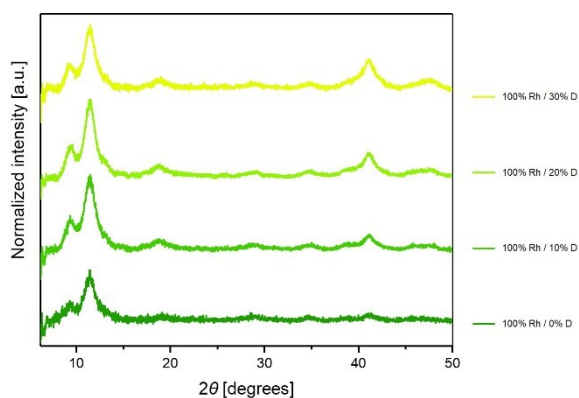


Figure S 3: PXRD patterns of 100%Rh pristine and TDE-materials indicating preserved crystallinity and increasing scattering of nanoparticles. In combination with TEM images, existing small NPs merge into larger ones which increases their X-ray scattering.

Elemental Analysis & Surface Areas

Table S 1: Found elementary contents, derived sum formulae, respective molecular weights, metal contents and nitrogen-based BET surface areas of all samples. *Based on duplicate analyses.

Sample	Found C*,H*,Cl,M _{total} values [wt-%]	Calculated Sum Formulae	Molecular Weight [g mol ⁻¹]	Metal Content [%]	N ₂ Surface Area [m ² g ⁻¹]
(100 / 0)	29.1/1.56/0/41.0	[Rh ₃ (BTC) _{1.61} (OAc) _{1.89}]	753.35	41.0	1360
(100 / 10)	28.1/1.30/0/43.1	[Rh ₃ (BTC) _{1.22} (IPA) _{0.39} (OAc) _{1.34}]	704.08	43.1	1340
(100 / 20)	27.9/1.28/0/45.5	[Rh ₃ (BTC) _{0.86} (IPA) _{0.74} (OAc) _{1.01}]	669.74	45.5	1424
(100 / 30)	27.6/1.22/0/48.0	[Rh ₃ (BTC) _{0.61} (IPA) _{0.99} (OAc) _{0.64}]	637.14	48.0	1274
(50 / 0)	30.4/1.66/1.5/39.2	[Ru _{1.44} Rh _{1.56} (BTC) _{1.52} (OAc) _{2.69} Cl _{0.3}]	791.44	18.4 / 20.8	1211
(50 / 10)	30.0/1.26/1.5/40.4	[Ru _{1.44} Rh _{1.56} (BTC) _{1.36} (IPA) _{0.57} (OAc) _{1.03} Cl _{0.3}]	753.18	19.0 / 21.4	n.d.
(50 / 20)	28.9/1.26/1.5/42.8	[Ru _{1.44} Rh _{1.56} (BTC) _{0.64} (IPA) _{1.27} (OAc) _{0.64} Cl _{0.3}]	695.69	20.1 / 22.7	n.d.
(50 / 30)	28.26/1.22/1.45/44.8	[Ru _{1.44} Rh _{1.56} (BTC) _{0.54} (IPA) _{1.27} (OAc) _{0.52} Cl _{0.3}]	667.45	21.0 / 23.7	n.d.
(0 / 0)	29.8/1.34/3.0/37.4	[Ru ₃ (BTC) _{1.89} (OAc) _{1.55} Cl _{0.7}]	810.73	37.4	1018
(0 / 10)	29.1/1.67/3.0/39.1	[Ru ₃ (BTC) _{0.56} (IPA) _{1.32} (OAc) _{1.55} Cl _{0.65}]	751.88	39.1	1065
(0 / 20)	30.8/0.93/2.9/41.2	[Ru ₃ (BTC) _{0.82} (IPA) _{1.44} (OAc) ₀ Cl _{0.61}]	730.18	41.2	1034
(0 / 30)	28.8/1.04/2.9/43.6	[Ru ₃ (BTC) _{1.12} (IPA) _{0.76} (OAc) _{0.24} Cl _{0.57}]	695.75	43.6	1173
Ru ^{II} -BTC	27.4/1.50/0/42.5	[Ru ₃ (BTC) _{1.32} (OAc) _{2.22}]	707.28	42.5	1493

Table S 2: Quantification of the term "defectiveness" in TDE samples depending on metal type and reference.

Sample	(XX/YY) Nomenclature		Removed wt-%	Removed Fraction of:		
	XX % Rh	YY %* Defects		Total Organics	Total Ligands	CO ₂ ⁻
(0/0)	0	0	0		0%	0%
(0/10)	0	10	5.50%	-9%	-18%	-19%
(0/20)	0	20	10%	-16%	-25%	-26%
(0/30)	0	30	15%	-24%	-28%	-29%
(50/0)	50	0	0		0%	0%
(50/10)	50	10	5.50%	-9%	-13%	-14%
(50/20)	50	20	10%	-16%	-28%	-30%
(50/30)	50	30	15%	-25%	-34%	-35%
(100/0)	100	0	0		0%	0%
(100/10)	100	10	5.50%	-9%	-14%	-14%
(100/20)	100	20	10%	-17%	-25%	-25%
(100/30)	100	30	15%	-25%	-34%	-34%

Predefined

Based on TGA / sum formulae

N₂ Sorption Isotherms & Pore Size Distributions

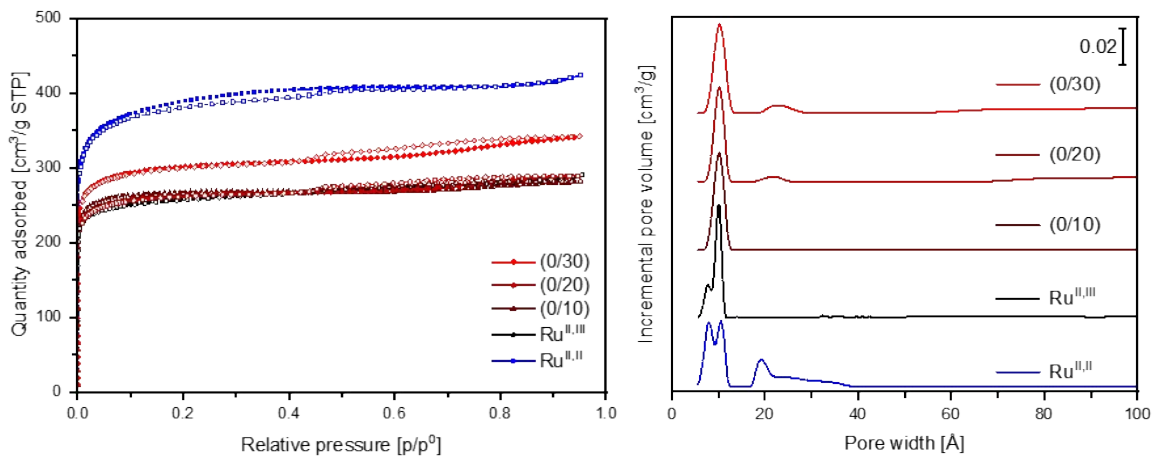


Figure S 4: Left: Nitrogen sorption isotherms of 0%Rh samples and Ru^{II,III}-MOF displaying both adsorption and desorption branches. Isotherms were recorded at 77K. Closed symbols represent data points from adsorption branch, open symbols represent data points from desorption branch. Hysteresis indicates upcoming mesoporosity. Right: Pore size distributions of ruthenium-based samples assuming cylindrical pores on oxide surfaces.

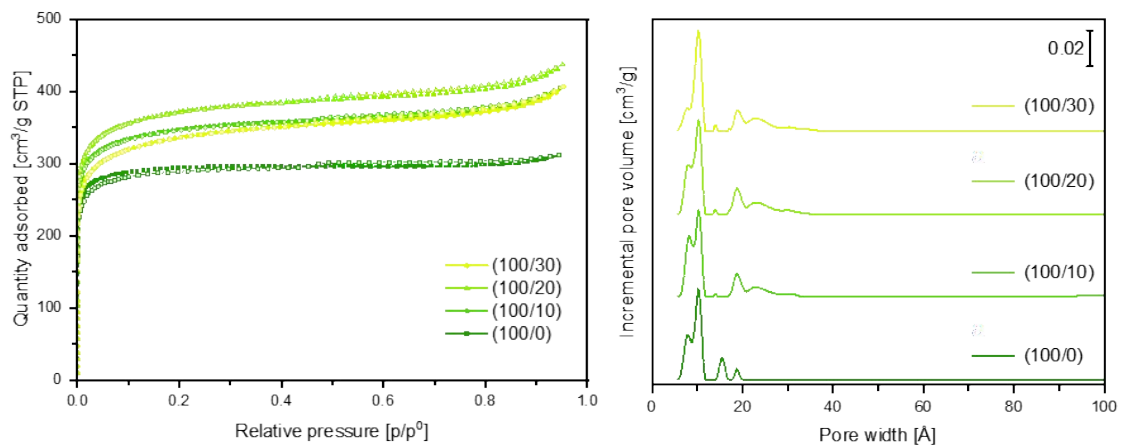


Figure S 5: Left: N₂ sorption isotherms for 100%Rh series recorded at 77K. Right: DFT-calculated pore size distributions assuming cylindrical pores on oxide surfaces. Increasing porosity emerges due to fusion of small sized micropores into larger pores.

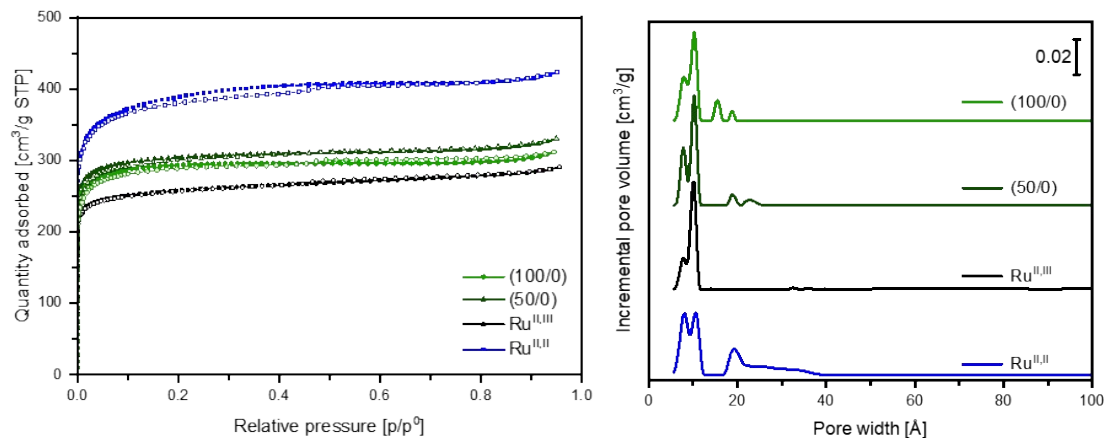


Figure S 6: Left: N₂ sorption isotherms for pristine Ru-, Rh- and bimetallic (50:50 Ru:Rh)-MOFs recorded at 77K. Right: DFT-calculated pore size distributions assuming cylindrical pores on oxide surfaces.

Thermogravimetric Analysis

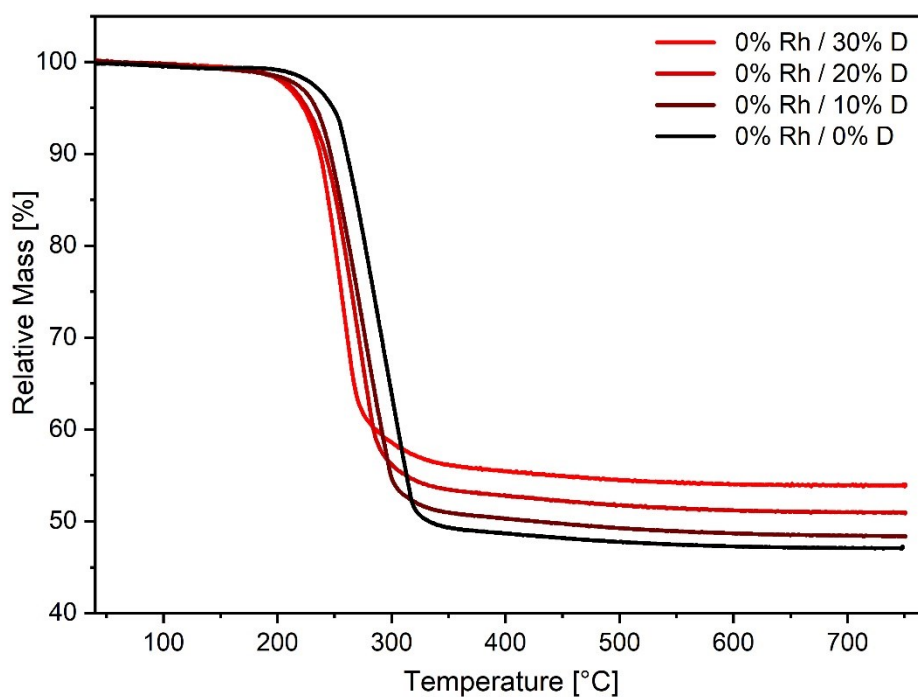


Figure S 7: TGA curves of 0%Rh samples (=Ru-MOF) with different defect amounts. Increasing metal oxide contents indicate successful TDE processes due to thermal organic constituent removal and allow for the metal content determination. Slightly decreased thermal stabilities may result from weakened structural stability of the defective frameworks.

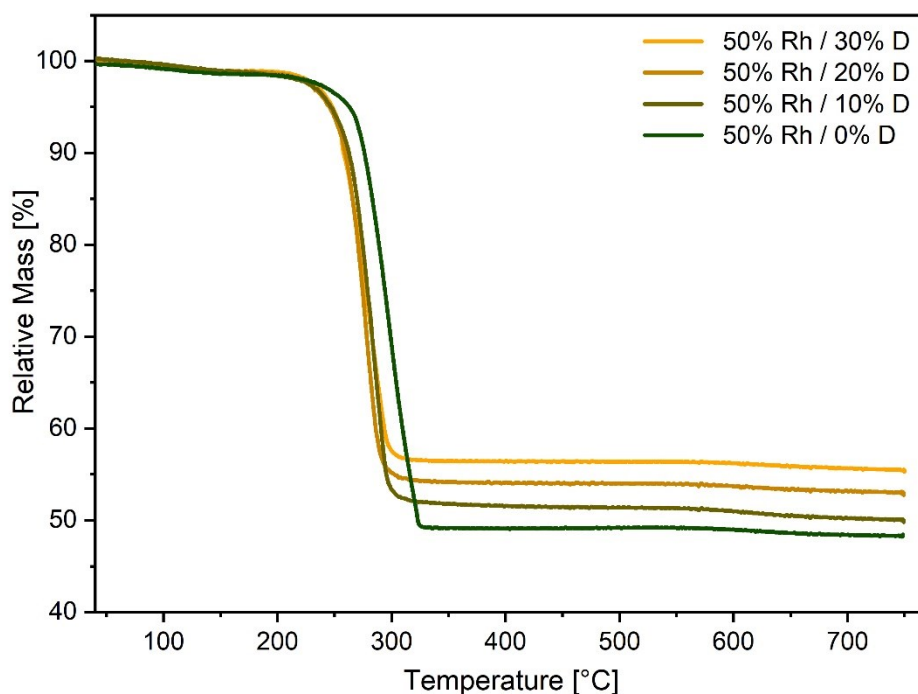


Figure S 8: TGA curves of 50%Rh samples with different defect amounts. Increasing metal oxide contents indicate successful TDE processes due to thermal organic constituent removal and allow for the metal content determinations. Slightly decreased thermal stabilities may result from weakened structural stability of the defective frameworks.

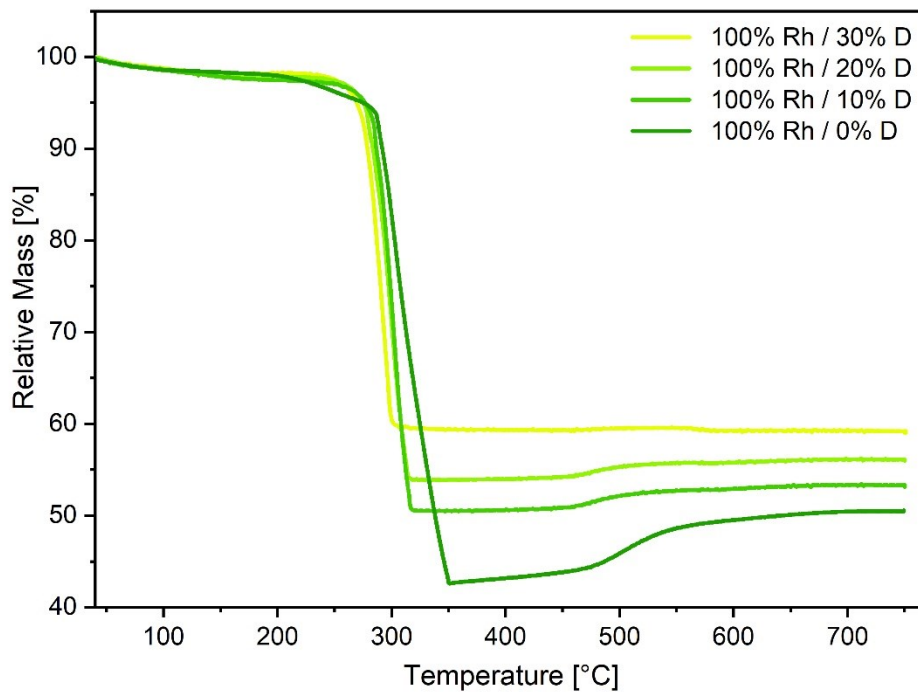


Figure S 9: TGA curves of 100%Rh samples with different defect amounts. Increasing metal oxide contents indicate successful TDE processes due to thermal organic constituent removal and allow for metal content determinations. Slightly decreased thermal stabilities may result from weakened structural stability of the defective frameworks. The weight increase at ~500°C results from reoxidation of elemental rhodium to Rh_2O_3 .

FT-IR spectroscopy

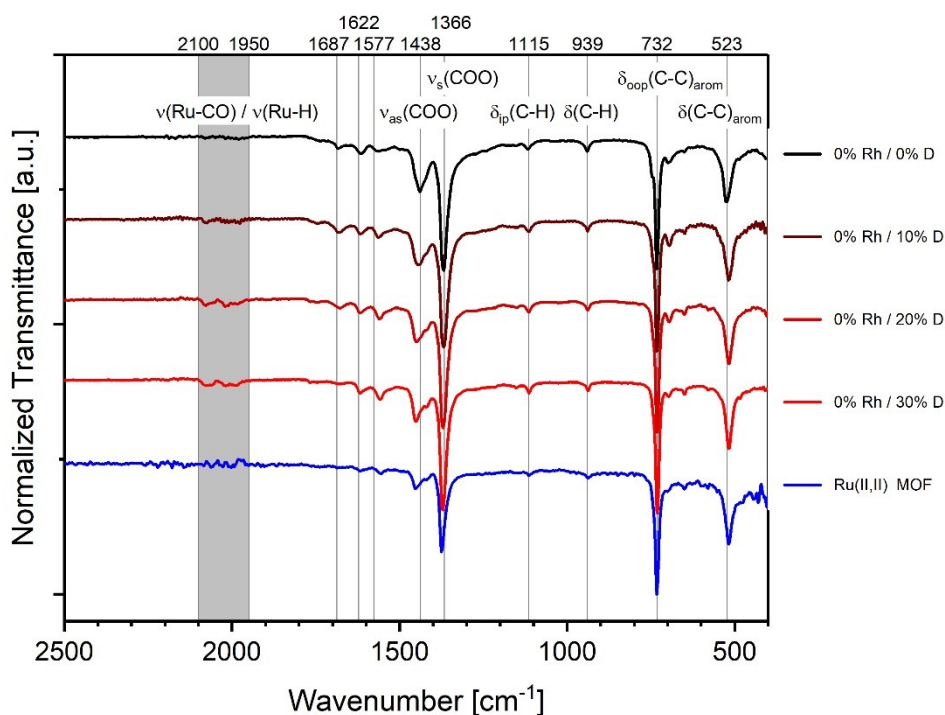


Figure S 10: Stacked FT-IR spectra of 0%Rh samples (pristine and TDE samples, Ru^{II,II}-BTC reference sample). Spectra reveal the formation of metal hydride and carbonyl species (1950 – 2100 cm⁻¹). A subsequent shift of $\nu_{as}(COO)$ (1438 cm⁻¹) and occurrence of a slight shoulder indicates metal reduction upon thermal defect-engineering e.g. through axial ligand removal.

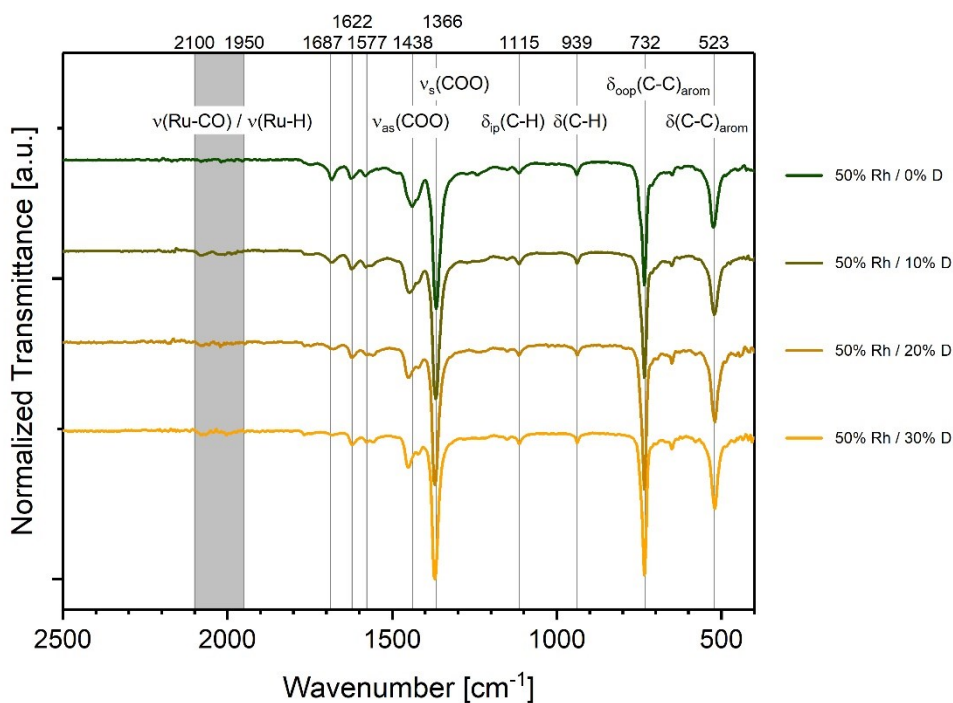


Figure S 11: Stacked FT-IR spectra of 50%Rh samples (pristine and TDE samples).

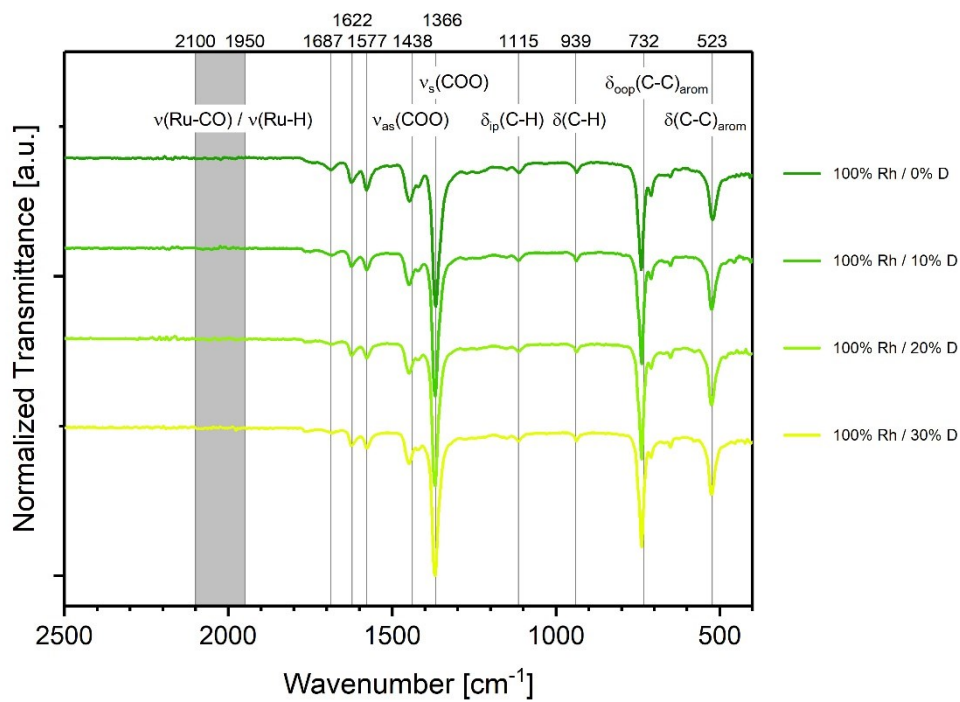


Figure S 12: Stacked FT-IR spectra of 100%Rh samples (pristine and TDE samples). Spectra do not reveal metal hydride or carbonyl formation with rhodium.

Raman Spectroscopy

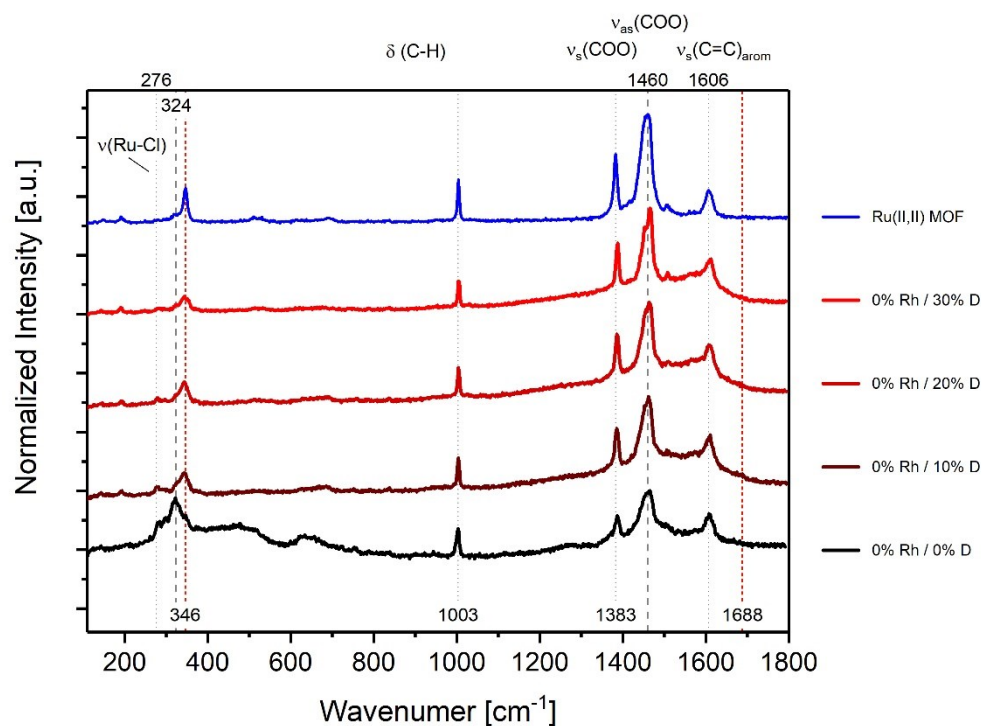


Figure S 13: Stacked Raman spectra of 0%Rh samples (pristine, TDE and Ru^{II,III} reference sample). Spectra reveal slight reduction of Ru-Cl bands (276 cm⁻¹) and removal of axial Ru-OAc species (324 cm⁻¹) suggesting partial metal reduction through axial ligand removal.

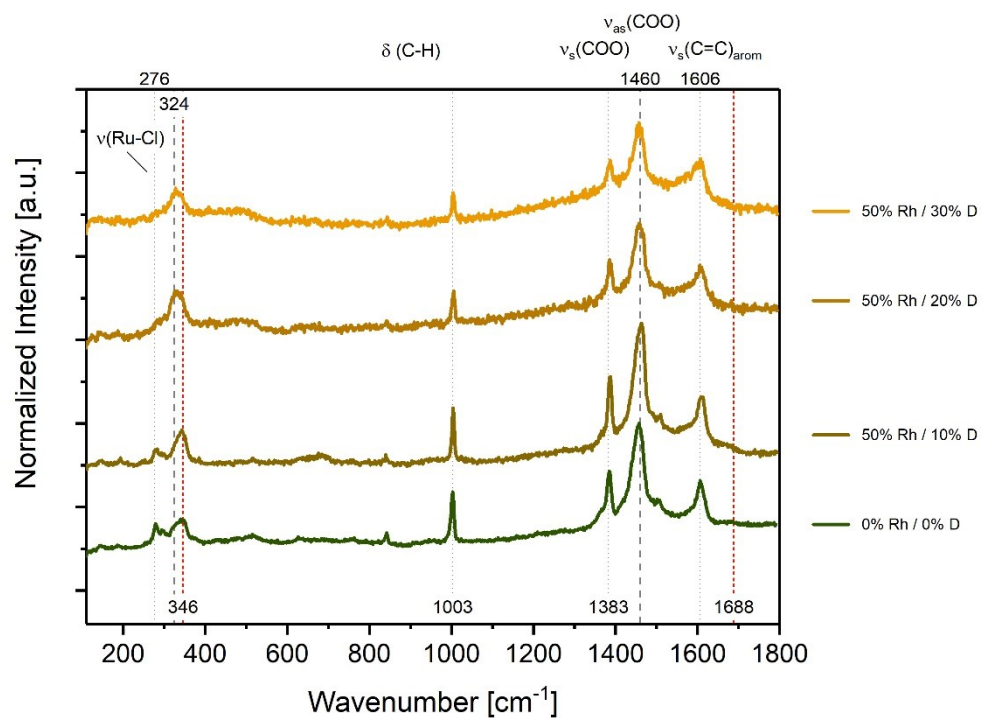


Figure S 14: Stacked Raman spectra of 50%Rh samples (pristine and TDE samples). Spectra reveal slight reduction of Ru-Cl bands (276 cm⁻¹) and removal of axial Ru-OAc species (324 cm⁻¹) suggesting partial metal reduction through axial ligand removal. Effects are considerably weaker compared with 0%Rh samples.

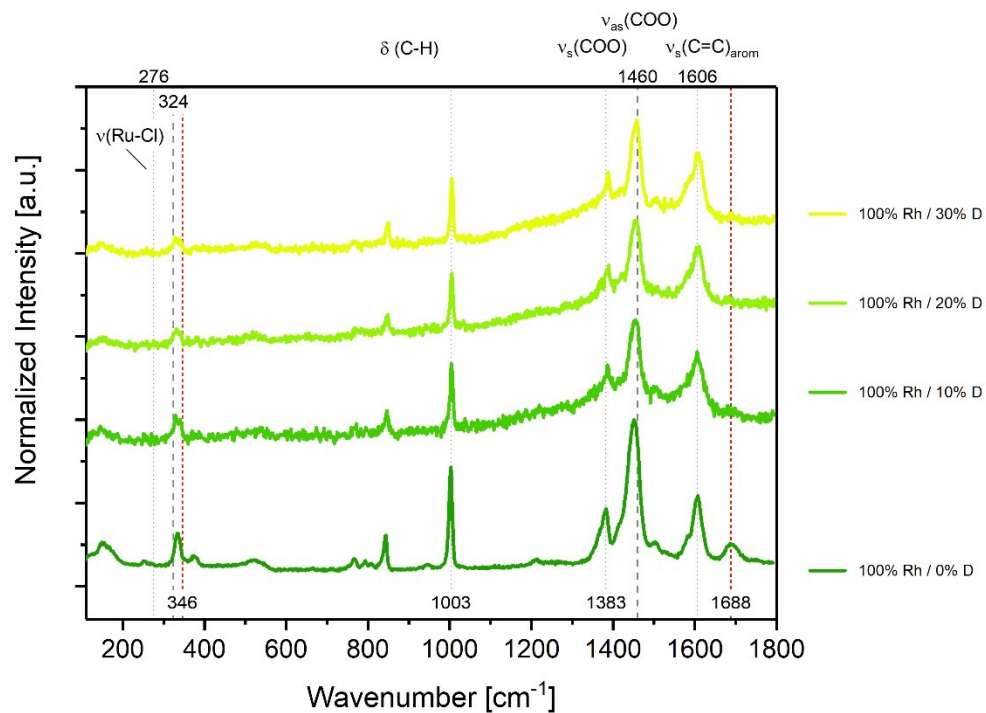


Figure S 15: Stacked Raman spectra of 100%Rh samples (pristine and TDE samples). Spectra reveal the removal of free carboxylates (1688 cm^{-1}) as well as a significant line broadening of aromatic C=C stretching modes (1606 cm^{-1}) indicating BTC decarboxylation towards isophthalate upon TDE.

TGA-Based Titration of OMS using CO

In the following, a graph summarizing the findings of the CO titration experiment using TGA is shown first. The entire, individual TGA curves are displayed then. Finally, quantitative values extracted from these experiments on the amounts of bound CO molecules per PW is shown in a table.

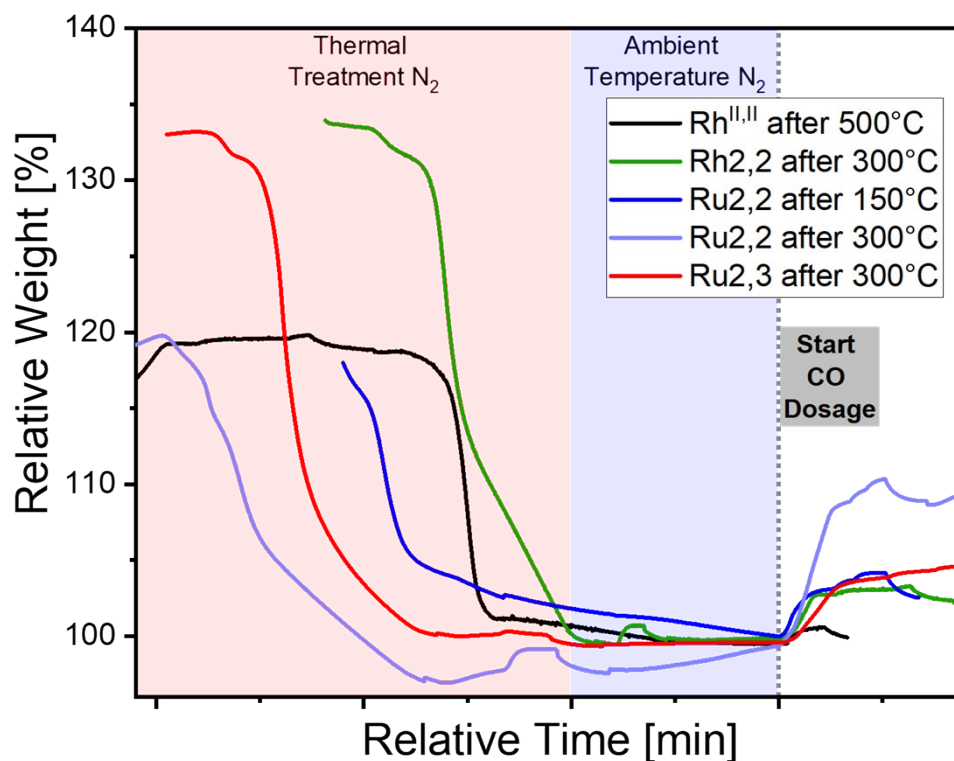


Figure S 16: TGA curves for CO-based titration experiments of selected MOF samples supporting an increased number of OMS upon thermal treatment. The investigated materials gave the following molecules CO per PW (treatment temperature in brackets): $Rh^{II,III}$ (300°C) 0.59, $Ru^{II,III}$ (300°C) 0.97, $Ru^{II,III}$ (150°C) 0.72, $Ru^{II,III}$ (300°C) 1.86. Note, the time of each experiment was adjusted to the start of CO dosage irrespective of the varying sample pretreatment. Relative weights are referenced to the start of the CO dosage as 100 wt-%.

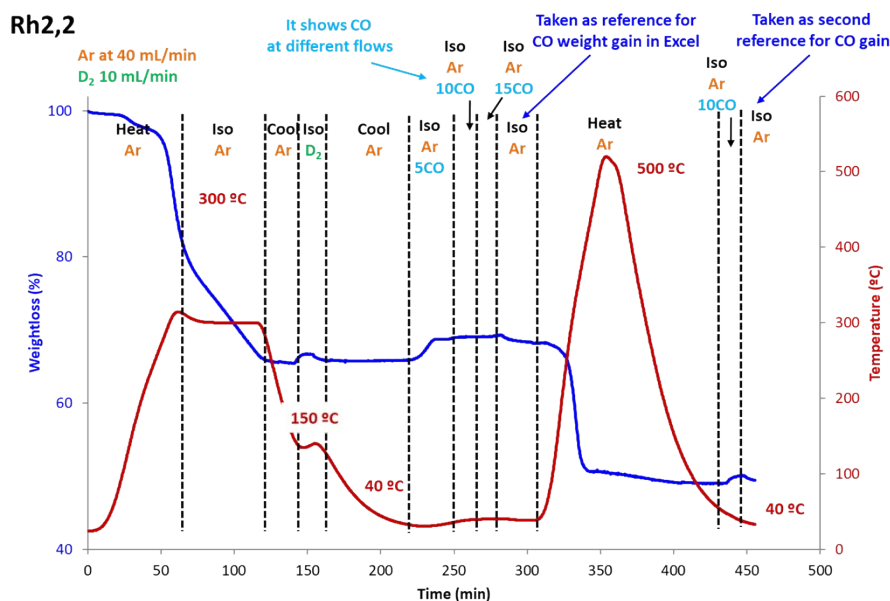


Figure S 17: TGA-based CO titration experiment with Rh-BTC treated at 300 °C. Weight curve (blue) and temperature program curve (red) with different gas streams (displayed on top). CO gas streams are given in mL/min. D_2 treatment serves for additional defect creation. The CO induced weight gain represents sorption of 0.30 molecules CO per metal atom. This refers

to roughly one CO rather strongly bound to a PW indicating the little weaker interaction of CO with Rh compared to Ru-BTC. As a reference, the sample was completely pyrolyzed at 500°C to exclusively form Rh NPs and load them with CO respectively. The then much smaller uptake of CO confirms the presence of active Rh sites after treatment at 300 °C.

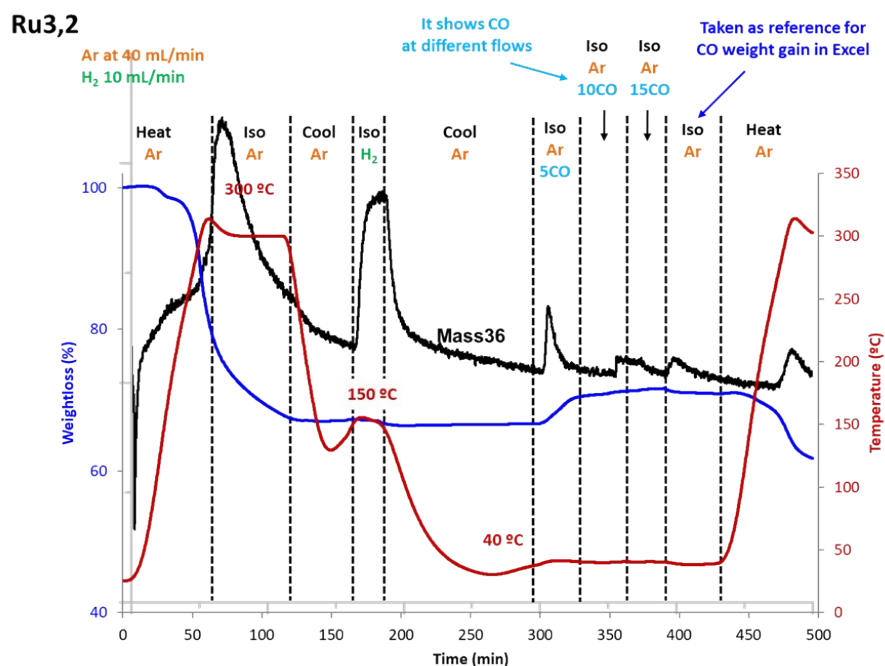


Figure S 18: TGA-based CO titration experiment with mixed-valent $Ru^{II,III}$ -BTC treated at 300 °C. CO gas streams are given in mL/min. Weight curve (blue) and temperature program curve (red) with different gas streams (displayed on top). H_2 treatment serves for additional defect creation and shows the release of axial chlorides. The CO induced weight gain represents sorption of 0.48 molecules CO per metal atom. This translates to one CUS per PW.

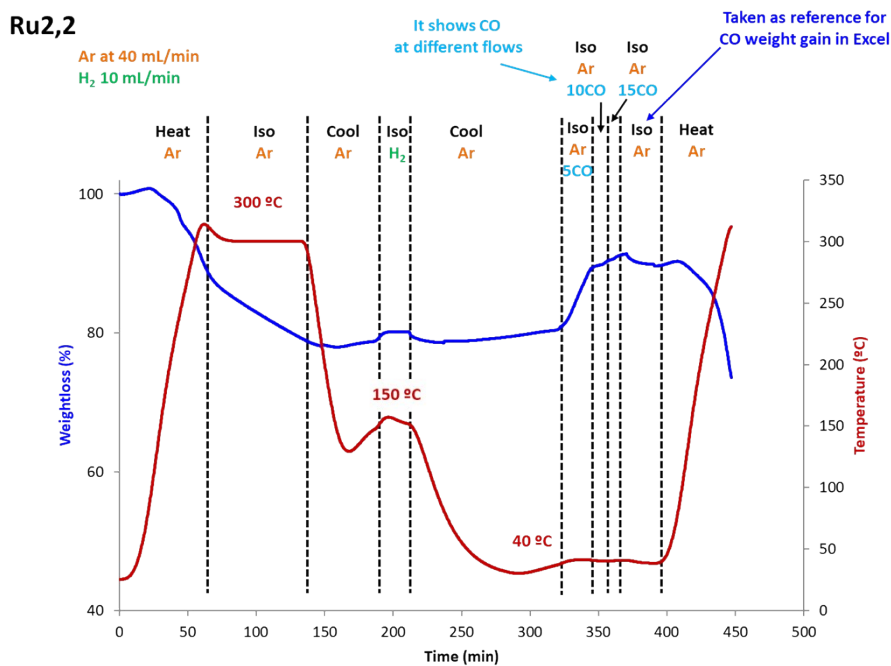


Figure S 19: TGA-based CO titration experiment with mixed-valent $Ru^{II,III}$ -BTC treated at 300 °C. CO gas streams are given in mL/min. H_2 treatment serves for additional defect creation. Weight curve (blue) and temperature program curve (red) with different gas streams (displayed on top). The CO induced weight gain represents sorption of 0.93 molecules CO per metal atom. This translates to two CUS per PW.

Ru^{II,II}

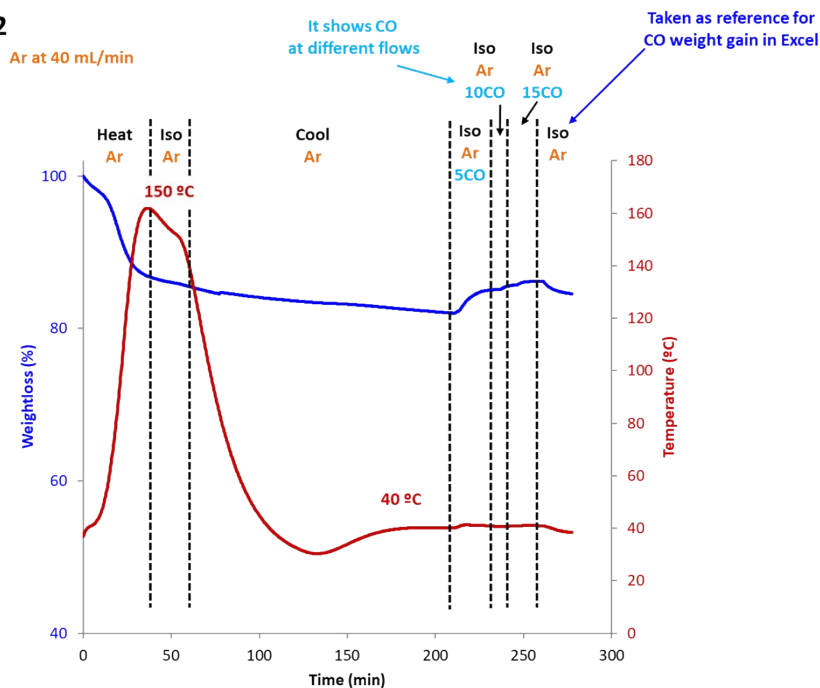


Figure S 20: TGA-based CO titration experiment with univalent Ru^{II,II}-BTC treated at 150 °C. CO gas streams are given in mL/min. Weight curve (blue) and temperature program curve (red) with different gas streams (displayed on top). The CO induced weight gain represents sorption of 0.36 molecules CO per metal atom. This refers to roughly one CO molecule rather strongly bound to a PW.

Table S 3: Summarized CO uptake per PW of each MOF system and respective pretreatment conditions.

MOF system	Pretreatment temperature [°C]	CO uptake per PW
Rh ^{II,II}	300	0.59
Ru ^{II,III}	300	0.97
Ru ^{II,II}	300	1.86
Ru ^{II,II}	150	0.72

Transmission Electron Microscopy

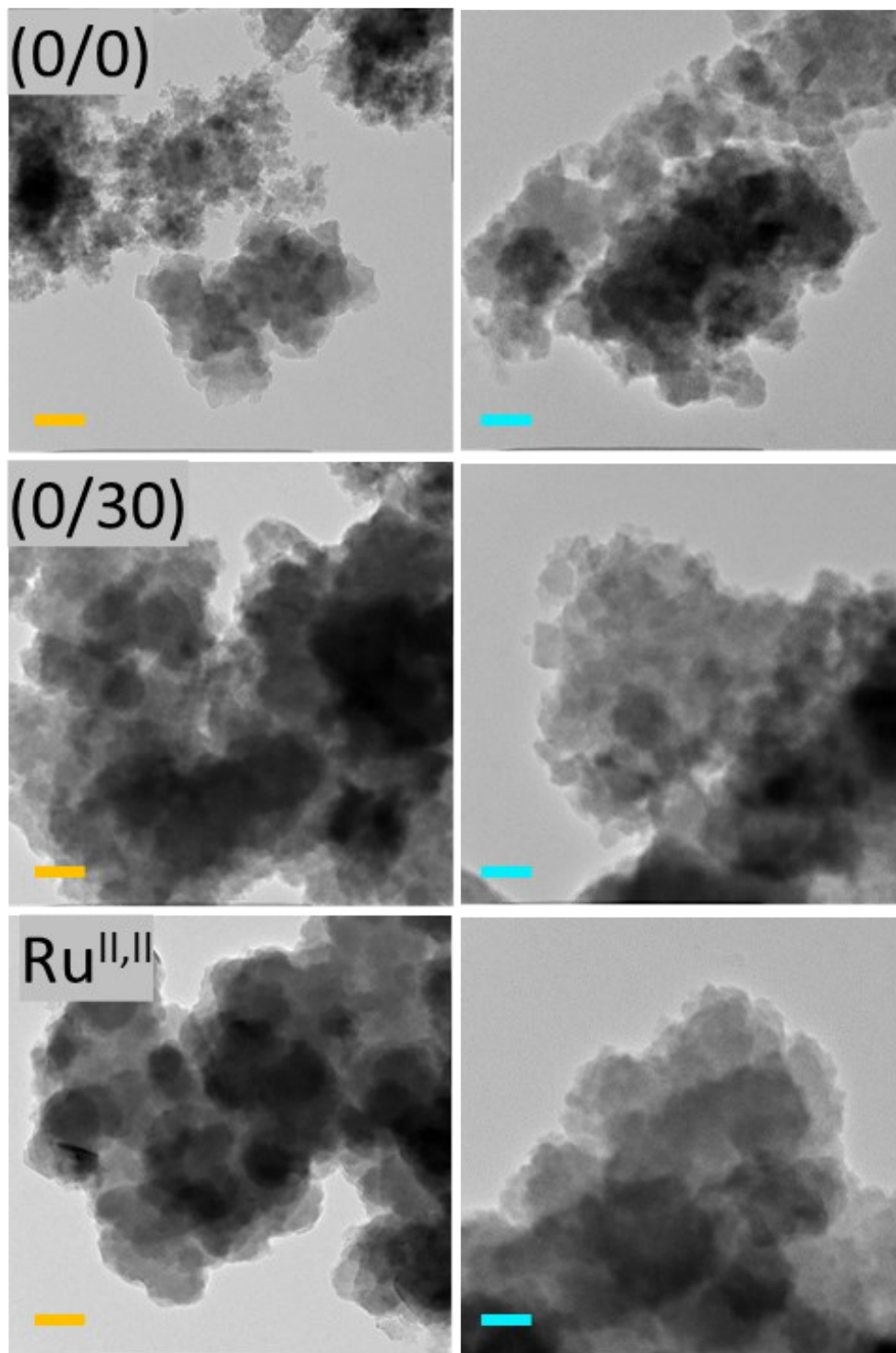


Figure S 21: HR-TEM images of ruthenium-based MOFs samples. Yellow scale bars represent 100 nm, blue ones 50 nm.

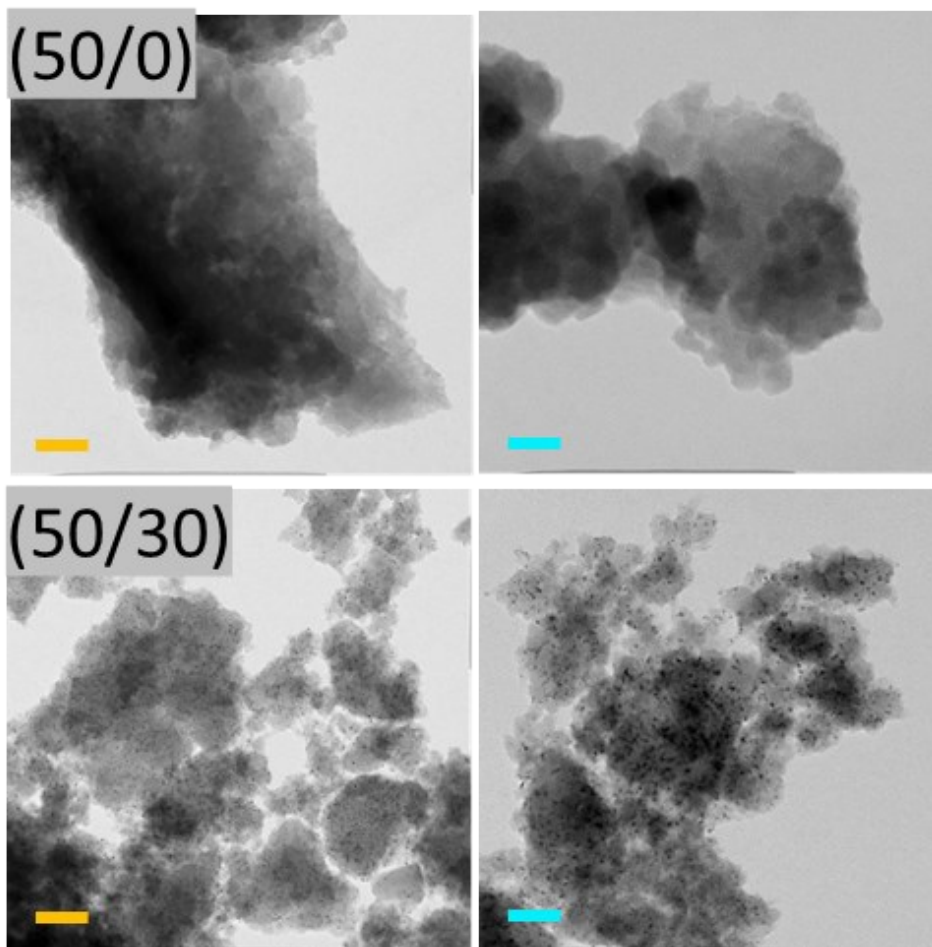


Figure S 22: HR-TEM images of 50% Rh MOFs samples. Yellow scale bars represent 100 nm, blue ones 50 nm. While pristine 50% Rh MOF sample is free of detectable NPs, upon TDE homogeneously dispersed metal NPs are observable (50/30).

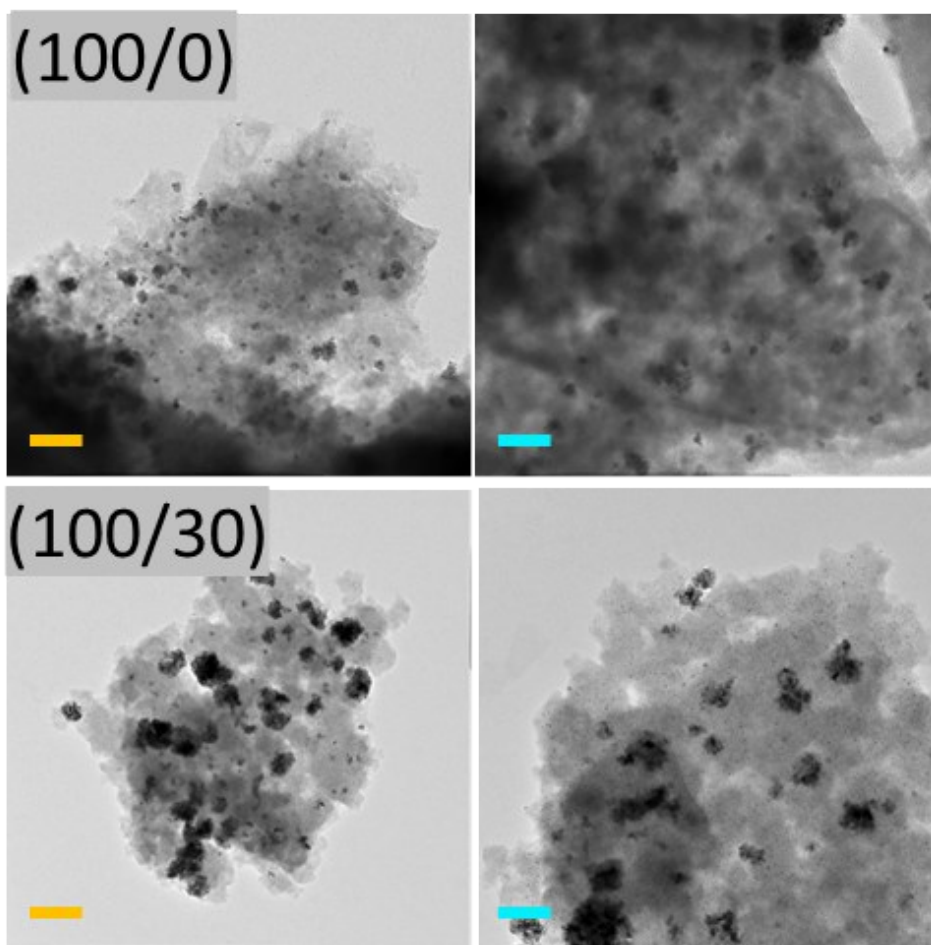


Figure S 23: HR-TEM images of 100% Rh MOFs samples. Yellow scale bars represent 100 nm, blue ones 50 nm. Presence of Rh NPs already in pristine MOFs (100/0), but increase upon TDE (100/30).

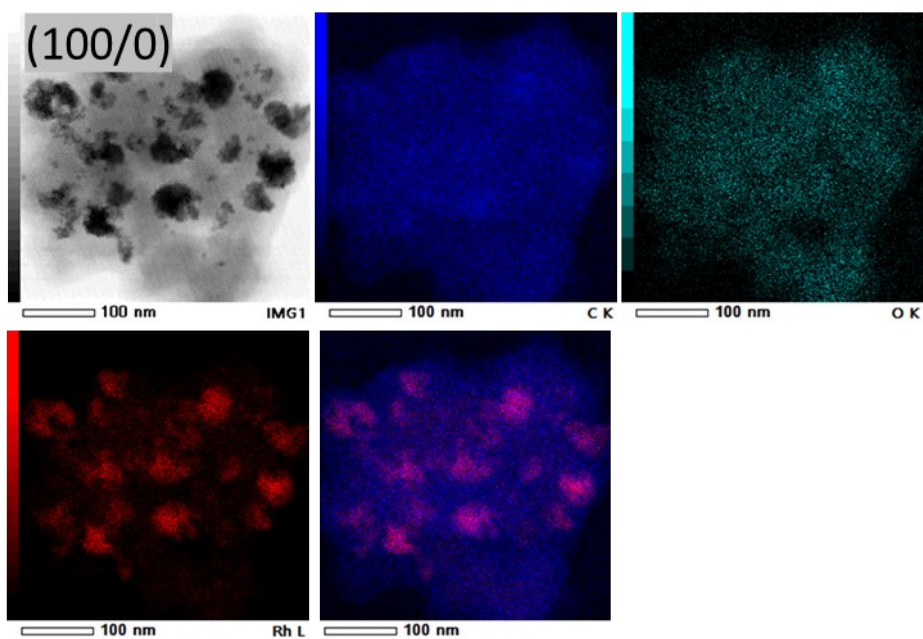


Figure S 24: Bright field STEM images of (100/0) sample and the respective EDX elemental mappings of C, O, Rh and an overlay of C&Rh (bottom middle) indicating a homogeneous MOF matrix with incorporated metal NPs.

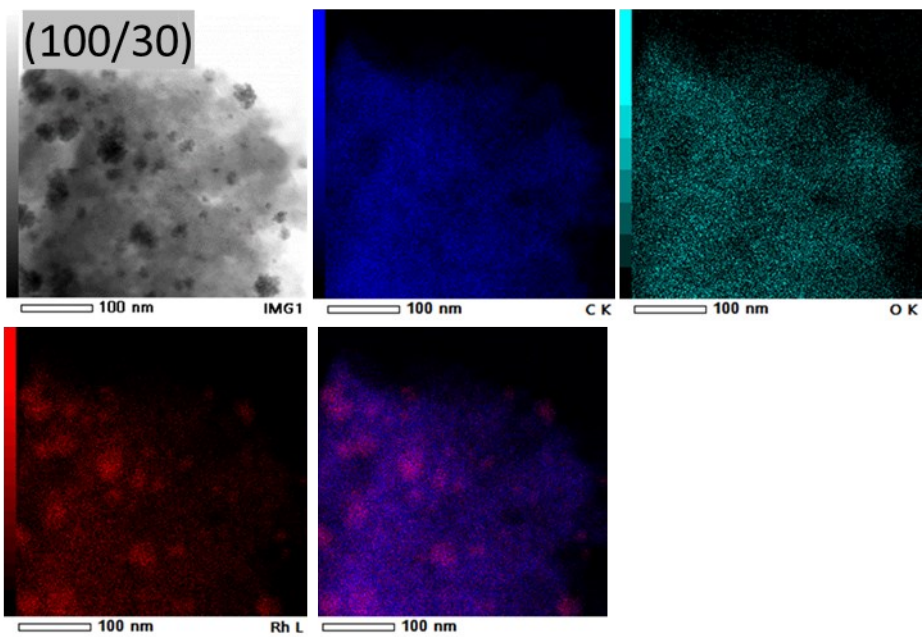


Figure S 25: Bright field STEM images of (100/30) sample and the respective EDX elemental mappings of C, O, Rh and an overlay of C&Rh (bottom middle) indicating a homogeneous MOF matrix with incorporated metal NPs.

Additional Information – Cyclopropanation Catalysis

Mechanistic Aspects relevant for this Study

This paragraph should provide the interested reader with additional background knowledge on the mechanisms and important parameters of the cyclopropanation reaction as briefly mentioned in the introduction of the main manuscript.

It is general knowledge that transition metal carbenoids play an important role as active species or intermediates in many catalytic reactions, such as olefin metathesis, O-H, N-H and C-H bond activation just to name a few.^{3, 4} For PW complexes, the CP is probably the most investigated reaction. Almost any imaginary combination (both inter- and intramolecularly) of Rh-PW catalyst, diazo compound, and olefin was screened to achieve deeper mechanistic comprehension of important parameters.⁵

The first, rate-determining step (r.d.s.) of transition metal-catalyzed CP is the denitration of diazo compounds and formation of a metal-carbene, which then transfers the carbene to the olefin in an outer-sphere fashion, which is fast, since the carbenes are highly reactive. For the r.d.s. and the catalytic activity, respectively, the availability of open metal sites (OMS) is thus most decisive. For styrene and EDA as reactants, the nature of the equatorial PW ligands was found to guide the diastereoselectivity. While strongly binding electron-rich carboxylates or carbamates at the PW give 64-68% *trans* selectivity, electron-poor fluorinated carboxylates lack any preference with 50% *trans* selectivity.⁶ Labile ligands temporarily dissociate yielding defective PWs. At those defective or modified PWs, more trajectories for styrene to approach the carbene are possible obstructing higher diastereoselectivities.^{4, 6} In contrast, the steric demand of the carboxylates (like acetate, pivalate or benzoate) has only minor impact on diastereoselectivities since the PW-inherent square planar geometry spanned by the metal atom and its four adjacent O ligator atoms governs the diastereomeric preference and more distant side groups perpendicular to the axially bound carbene do not play a decisive role. Unwanted side-products resulting from homocoupling of two carbenes or from C-H activation are known to occur.³ Homocoupling is usually suppressed by process control *via* slow addition of a diluted EDA solution over time and the excessive use of olefin.⁷ Other side products can emerge from C-H activation of styrene.³ Such a carbene-transfer results in linear allyl species which are further denoted as linear products. Other, non-PW complexes are known to produce cyclopropanes and linear products in different ratios.^{8, 9} In contrast to the CP formation, these linear products could emerge via metallacyclobutane intermediates requiring additional OMS at the metal centre.^{3, 9} From this fact, we conclude that their formation (which is not observed in perfect PW systems like Rh₂(OAc)₄ or Cu₃(BTC)₂) is indicative for the presence of modified PWs in PGM-MOFs as presented earlier by several other analytical techniques.¹⁰

Additional Catalysis Data

Table S 4: Summary of catalysis data of all samples. Initial turnover frequencies (TOFs) are given in h^{-1} and are calculated as outlined above using 1.3 mol-% catalyst loading with respect to the total metal content and EDA. Chemoselectivities refer to conversions after 24 h. The given diastereoselectivity (DS) in % refers to the trans-cyclopropane. *The $\text{Rh}_2(\text{OAc})_4$ sample reached quantitative conversion already at the first measurement upon complete EDA addition. Thus, the TOF is experimentally limited to this value. **In contrast to all other MOF samples, the Ru and Rh NPs differed significantly in their 24h selectivity values compared to earlier data points. To avoid misinterpretation, both values are presented: 24 h values as similar to the other samples, 4 h values are marked with **.

Sample	TOF [h^{-1}]	Chemoselectivity of			DS of trans-CP [%]
		CPs [%]	Homo-coupling [%]	Linear products [%]	
(0/0)	49.9	68.7	29.3	2.0	56
(0/10)	64.2	70.3	27.6	2.0	54.4
(0/20)	83.8	77.4	20.9	1.8	55.2
(0/30)	92.3	81.0	17.0	2.0	55.4
Ru ^{II,II} -MOF	110.3	83.4	14.3	2.3	53.6
(50/0)	112	82.8	2.1	15.1	51.4
(50/10)	107.2	83.5	1.9	14.6	50.9
(50/20)	108.2	83.4	1.7	14.8	49.5
(50/30)	113.7	82.8	1.7	15.5	48
(100/0)	88	81.5	0.7	17.7	51
(100/10)	78	82.5	1.7	15.8	49.3
(100/20)	93.6	82.5	1.3	16.2	48.7
(100/30)	92.3	81.4	0	18.6	48.9
Cu-HKUST-1	18.2	83.7	16.3	0	65
$\text{Rh}_2(\text{OAc})_4$	145*	100	0	0	64.2
Ru NPs	11.3	83.6	16.4	0	61.8
Ru NPs**	11.3	69.4	30.6	0	60.1
Rh NPs	8.7	78.5	16.6	4.8	61.8
Rh NPs**	8.7	68.9	31.1	0	61.2

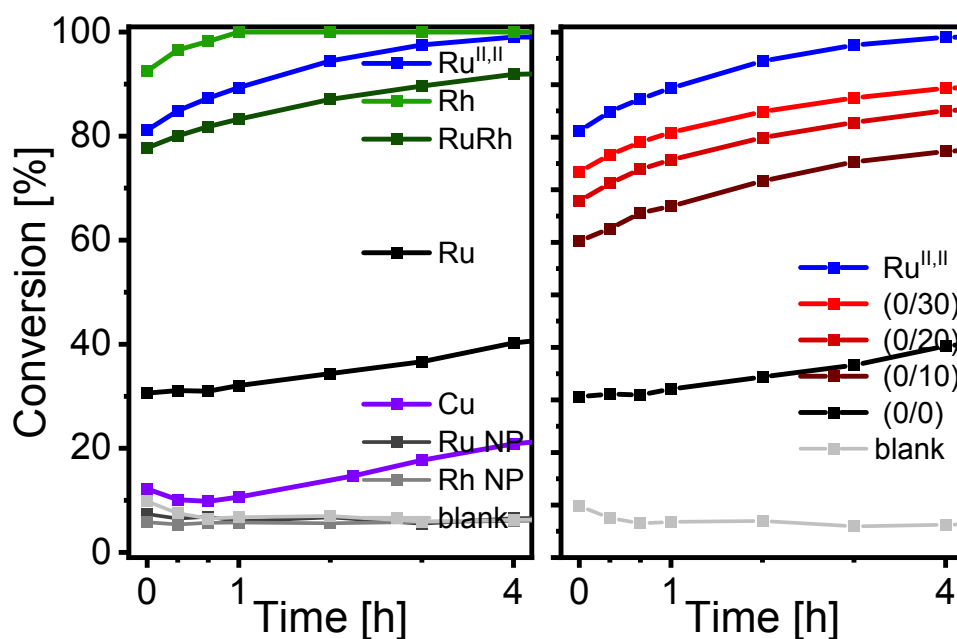


Figure S 26: Early activity in the cyclopropanation reaction of styrene with EDA. Left: Time conversion plots comparing different pristine HKUST-1 analogues of Cu (purple), Ru (mixed-valent (black) and univalent (blue)) and Rh (green) and respective NPs (grey) as catalysts. Right: Activity comparison of different ruthenium-based MOFs: The moderate activity of the mixed-valent $\text{Ru}^{\text{II,II}}$ -MOF (0/0) is strongly enhanced by TDE (0/10→30) (brown to red curves). This Figure contains the data from Figure 3 in the main text but highlights the evolution of conversion for the initial period. Sampling was repeated every 20 min within the first hour, and then on an hourly interval.

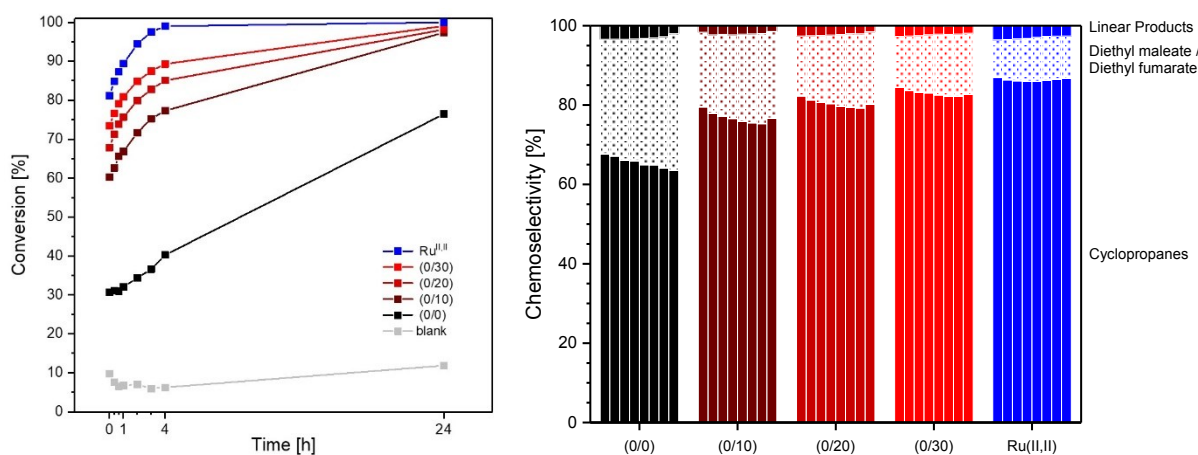


Figure S 27: Left: Time-Conversion plots for Ru-MOF samples (each 5 mg) and the blank reaction. The beneficial effect of TDE on Ru-MOF is clearly to be seen. $\text{Ru}^{\text{II,II}}$ -MOF exhibits the highest activity. Right: Stacked chemoselectivities for each data point within the series of Ru-MOFs. Each group represents the development during the reaction. The top fraction is for linear products, the middle for the homocoupling products, the bottom and main fraction are the cyclopropanes. A clear improvement of the selectivity towards CP products can be extracted. Homocoupling products represent the main side products. As TDE accounts for a successive removal of mostly axial ligands, their presence might account for the homocoupling side reaction.

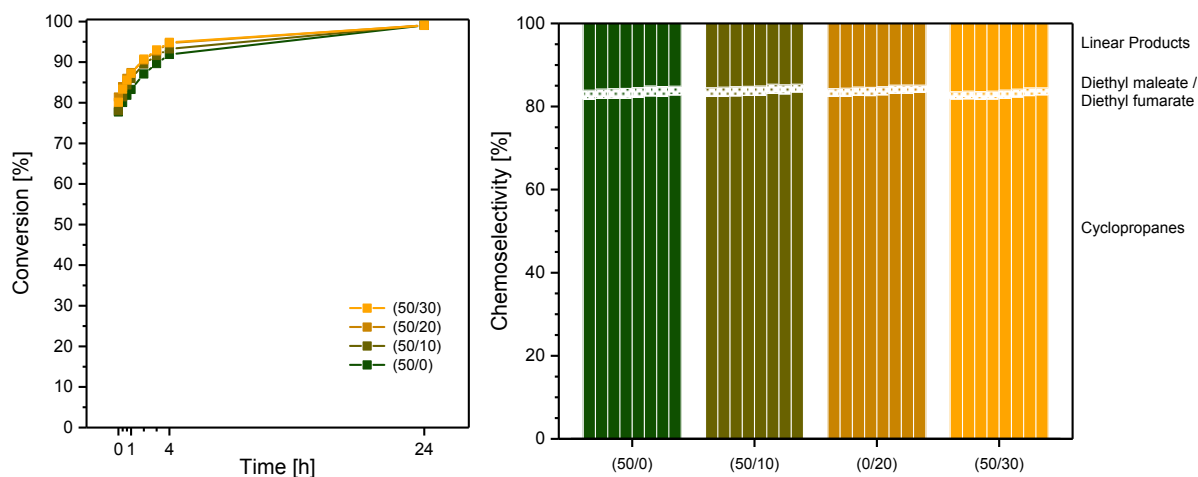


Figure S 28: Left: Time-Conversion plots for mixed-metallic RuRh-MOF samples (each 5 mg). Almost identical activity can be seen irrespective of the TDE. However, The (50/30) sample exhibits the highest activity. Right: Stacked chemoselectivities for each data point within the series of RuRh-MOFs. Each group represents the development during the reaction. The top fraction is for linear products, the middle for the homocoupling products, the bottom and main fraction are the cyclopropanes. Linear propene species account for the main side products from RuRh-MOF catalysis. The product distribution seems unaffected by TDE.

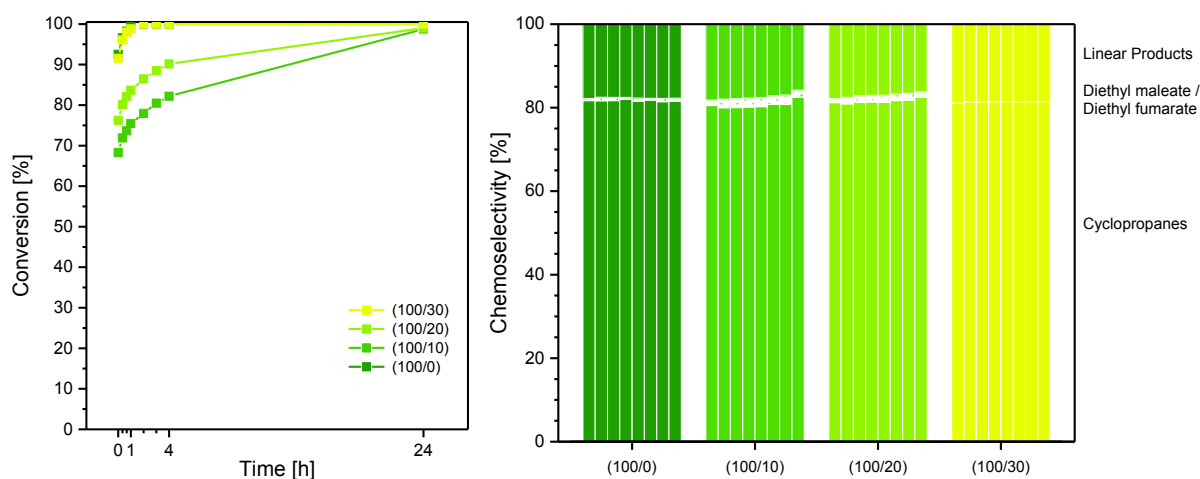


Figure S 29: Left: Time-Conversion plots for Rh-MOF samples (each 5 mg). A first activity drop for the (100/10) sample is visible with again rising activity for (100/20) and (100/30) samples. The (100/30) sample exhibits comparable activity as the pristine Rh-MOF. Right: Stacked chemoselectivities for each data point within the series of Rh-MOFs. Each group represents the development during the reaction. The top fraction is for linear products, the middle for the homocoupling products, the bottom and main fraction are the cyclopropanes. Linear propene species account for the main side products from RuRh-MOF catalysis. The product distribution seems unaffected by TDE.

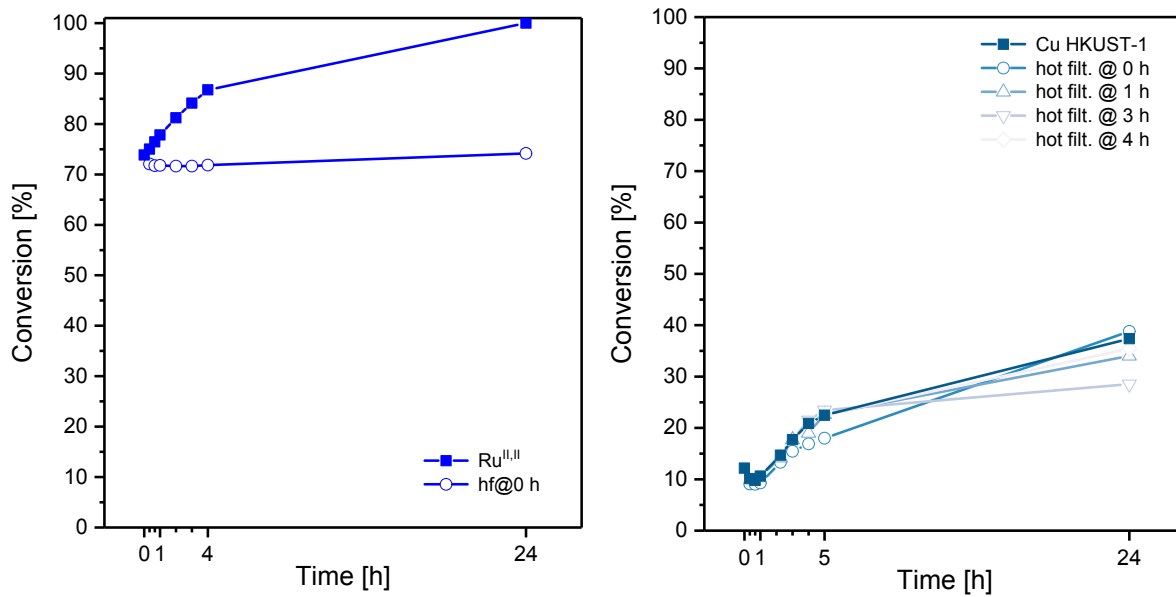


Figure S 30: Hot filtration experiments indicating the differences between Ru^{II,II}-MOF sample representing the precious-metal analogues of the parent Cu-HKUST-1 (depicted on the right). Cu-HKUST-1 exhibits significantly lower performance which can even be attributed to leaching species into the solutions as hot filtration tests performed after different reaction times clearly indicate. The Ru-MOF does not exhibit leaching. For both graphs, equal metal loadings of 1.3 mol-% were applied to allow comparable data.

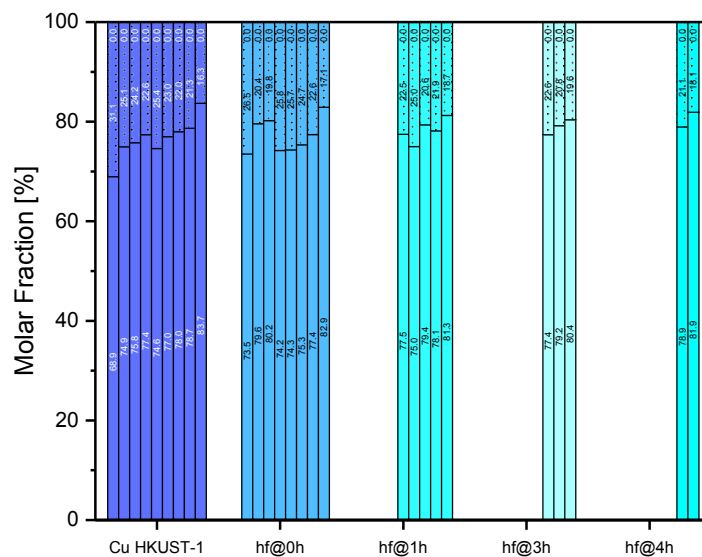


Figure S 31: Chemoselectivity of Cu-HKUST-1 and the respective hot filtration experiments with respect to the time-conversion plots of the right graph in Figure S 30.

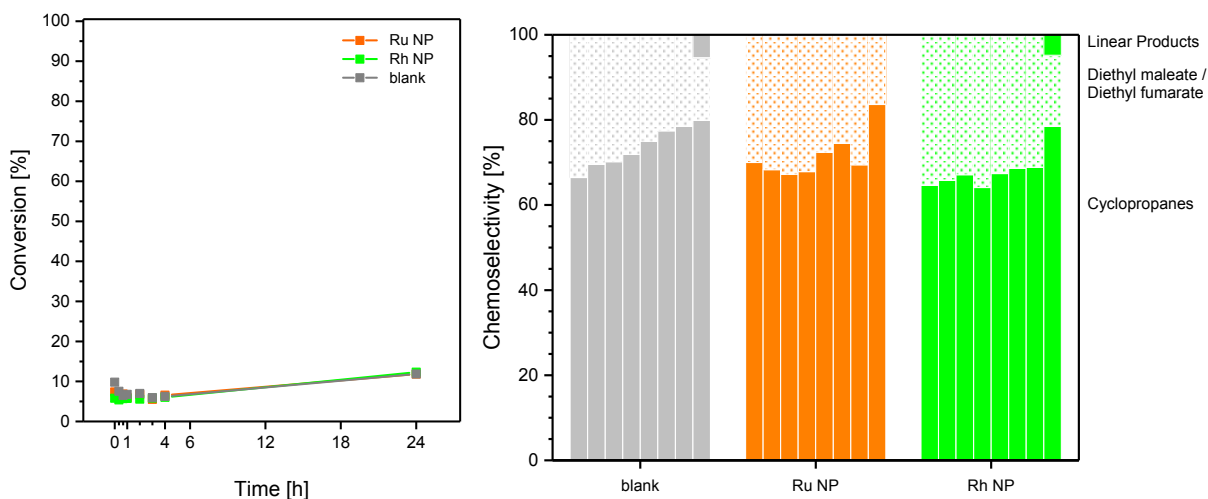


Figure S 32: Left: Time-conversion plots for metal nanoparticles and the blank reaction indicating the particles inactivity. Right: Chemoselectivity of blank and NPs in the course of the reaction indicating mostly the homocoupling as side reaction.

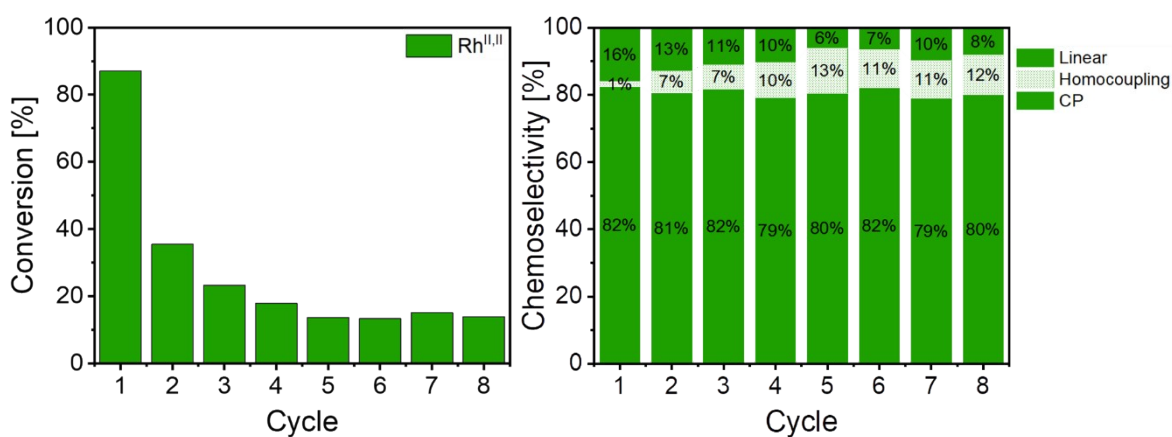


Figure S 33: Recycling of pristine Rh-MOF sample: Cycle dependent evolution of activity (left) and chemoselectivity (right). The data indicates reduced catalytic activity presumably due to pore blocking phenomena or competing adsorption of polar reaction products on OMS while the chemoselectivity of the catalyst remains mostly unaffected. Reduced linear product formation presumably due to regeneration of perfect PWs from modified PWs.

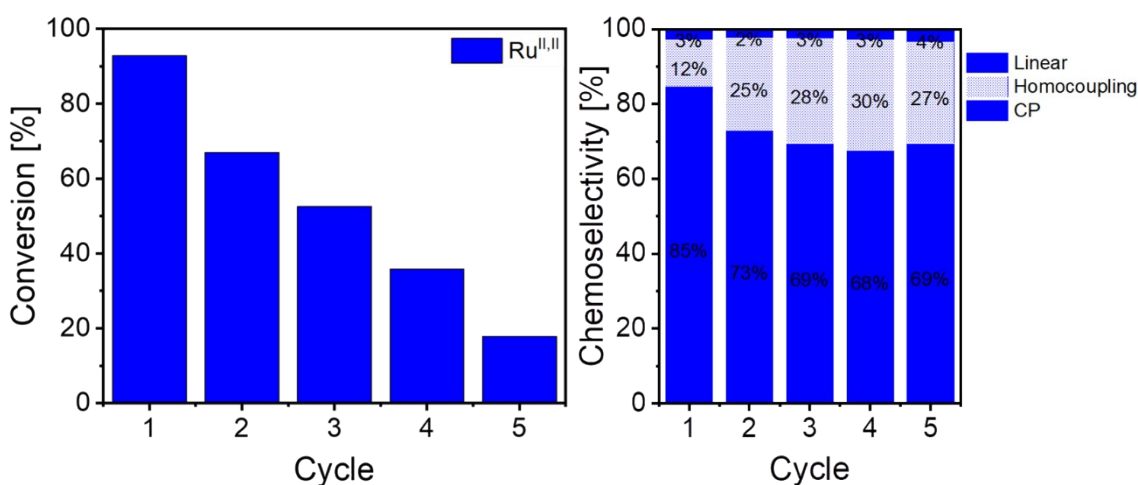


Figure S 34: Recycling of pristine Ru^{II,III}-MOF sample: Cycle dependent evolution of activity (left) and chemoselectivity (right). The data indicates reduced catalytic activity with cycling which can presumably be attributed to pore blocking phenomena or competing adsorption of polar reaction products on OMS. In contrast to Rh-BTC, the evolution of the chemoselectivity with

cycling indicates oxidation towards $Ru^{II,III}$ PWs displaying the reversed process of TDE. Thus the reduced activity also stems from oxidation and its concomitant reduction of OMS.

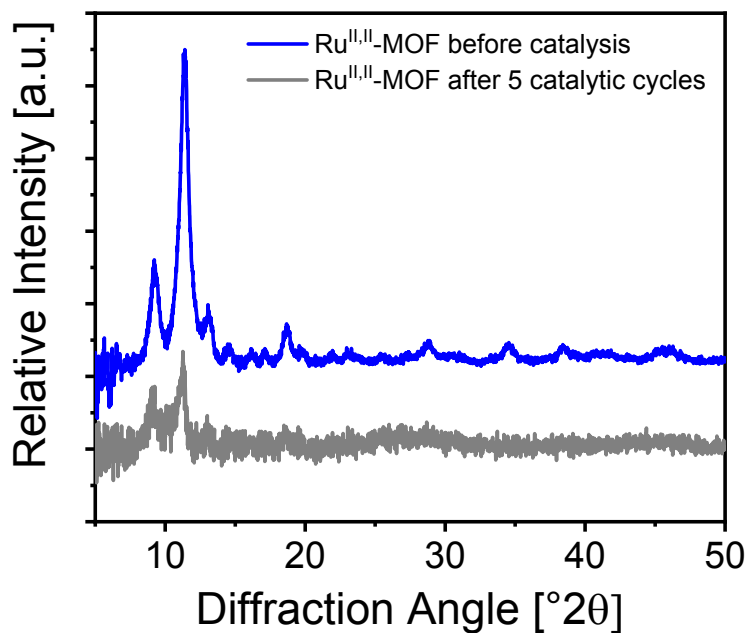
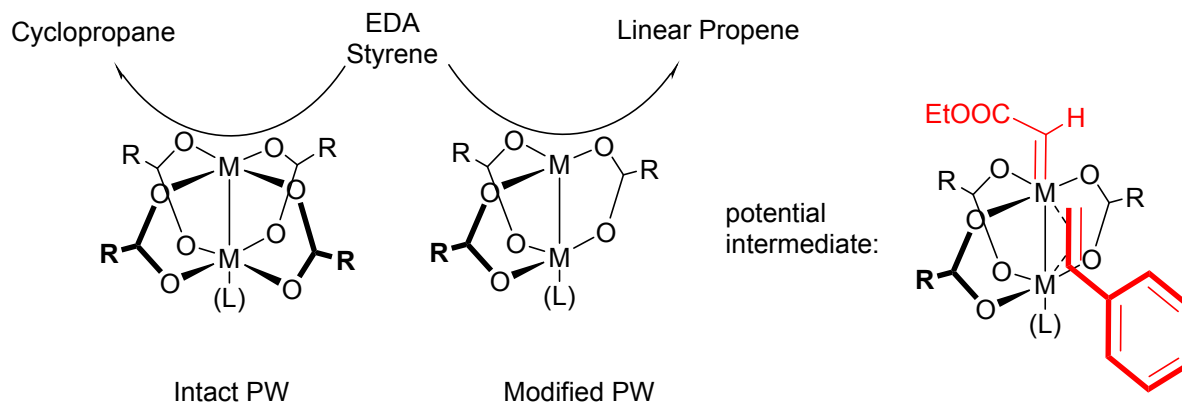


Figure S 35: PXRD pattern of univalent $Ru^{II,III}$ -MOF sample before and after catalysis indicating mostly preserved structural order. The low signal intensity and high level of noise is assigned to the very low sample amount available after catalysis.



Scheme S 3: Proposed intermediate for the formation of linear propene species observed in rhodium catalysed reactions. The formation presumably takes place on defective PWs offering two coordination sites.

1. R. W. Mitchell, A. Spencer and G. Wilkinson, *J. Chem. Soc., Dalton Trans.*, 1973, DOI: 10.1039/DT9730000846, 846-854.
2. W. R. Heinz, T. Kratky, M. Drees, A. Wimmer, O. Tomanec, S. Günther, M. Schuster and R. A. Fischer, *Dalton Trans.*, 2019, **48**, 12031-12039.
3. M. P. Doyle and D. Ren, in *Prog. Inorg. Chem.*, 2007, DOI: 10.1002/9780470166512.ch2, pp. 113-168.
4. M. P. Doyle, *J. Org. Chem.*, 2006, **71**, 9253-9260.
5. M. Brookhart and W. B. Studabaker, *Chem. Rev.*, 1987, **87**, 411-432; A. Padwa, D. J. Austin, S. F. Hornbuckle, M. A. Semones, M. P. Doyle and M. N. Protopopova, *J. Am. Chem. Soc.*, 1992, **114**, 1874-1876; M. P. Doyle, L. J. Westrum, W. N. E. Wolthuis, M. M. See, W. P. Boone, V. Bagheri and M. M. Pearson, *J. Am. Chem. Soc.*, 1993, **115**, 958-964; M. P. Doyle and D. C. Forbes, *Chem. Rev.*, 1998, **98**, 911-936.
6. A. J. Anciaux, A. J. Hubert, A. F. Noels, N. Petiniot and P. Teyssie, *J. Org. Chem.*, 1980, **45**, 695-702.
7. K. Epp, B. Bueken, B. Hofmann, M. Cokoja, K. Hemmer, D. E. De Vos and R. A. Fischer, *Catal. Sci. Technol.*, 2019, **9**, 6452-6459.
8. G. Maas, *Chem. Soc. Rev.*, 2004, **33**, 183-190; F. A. Cotton, K. R. Dunbar and M. G. Verbruggen, *J. Am. Chem. Soc.*, 1987, **109**, 5498-5506; F. Simal, A. Demonceau, A. F. Noels, D. R. T. Knowles, S. O'Leary, P. M. Maitlis and O. Gusev, *J. Organomet. Chem.*, 1998, **558**, 163-170.
9. A. F. Noels and A. Demonceau, *J. Phys. Org. Chem.*, 1998, **11**, 602-609.
10. W. R. Heinz, I. Aguirrezabal-Telleria, R. Junk, J. Berger, J. Wang, D. I. Sharapa, M. Gil-Calvo, I. Luz, M. Soukri, F. Studt, Y. Wang, C. Wöll, H. Bunzen, M. Drees and R. A. Fischer, *ACS Appl. Mater. Interfaces*, 2020, DOI: 10.1021/acsami.0c10721.